

Discovery of radio halos and double-relics in distant MACS galaxy clusters: clues to the efficiency of particle acceleration.

A. Bonafede^{1,2*}, M. Brüggen^{1,2}, R. van Weeren^{3,4}, F. Vazza^{1,2}, G. Giovannini^{5,6}
H. Ebeling⁷, A. C. Edge⁸, M. Hoeft⁹, U. Klein¹⁰

¹Jacobs University Bremen, Campus Ring 1, D-28759 Bremen, Germany.

²Hamburger Sternwarte, Universität Hamburg, Gojenbergsweg 112, 21029, Hamburg, Germany.

³Netherlands Institute for Radio Astronomy (ASTRON), Post-bus 2, 7990 AA Dwingeloo, the Netherlands.

⁴Leiden Observatory, Leiden University, P.O. Box 9513, NL-2300 RA Leiden, The Netherlands.

⁵INAF Istituto di Radioastronomia, via P. Gobetti 101, I-40129 Bologna, Italy.

⁶Università di Bologna, Dip. di Astronomia, via Ranzani 1, I-40126 Bologna, Italy.

⁷Institute for Astronomy, University of Hawaii, 2680 Woodlawn Drive, Honolulu, HI 96822, USA.

⁸Department of Physics, Durham University, Durham DH1 3LE, United Kingdom.

⁹Thüringer Landessternwarte, Sternwarte 5, 07778 Tautenburg, Germany.

¹⁰Argelander-Institut für Astronomie, Auf dem Hügel 71, D-53121 Bonn, Germany.

Received ; accepted

ABSTRACT

We have performed 323 MHz observations with the Giant Metrewave Radio Telescope of the most promising candidates selected from the MACS catalog. The aim of the work is to extend our knowledge of the radio halo and relic populations to $z > 0.3$, the epoch in which massive clusters formed. In MACSJ1149.5+2223 and MACSJ1752.1+4440, we discovered two double-relic systems with a radio halo, and in MACSJ0553.4-3342 we found a radio halo. Archival Very Large Array observations and Westerbork Synthesis Radio Telescope observations have been used to study the polarization and spectral index properties. The radio halo in MACSJ1149.5+2223 has the steepest spectrum ever found so far in these objects ($\alpha \geq 2$). The double relics in MACSJ1149.5+2223 are peculiar in their position that is misaligned with the main merger axis. The relics are polarized up to 30% and 40% in MACSJ1149.5+2223 and MACSJ1752.040+44, respectively. In both cases, the magnetic field is roughly aligned with the relics' main axes. The spectra in the relics in MACSJ1752.040+44 steepen towards the cluster centre, in agreement with model expectations. X-ray data on MACSJ0553.4-3342 suggests that this cluster is undergoing a major merger, with the merger axis close to the plane of the sky. The cores of the disrupted clusters have just passed each other, but no radio relic is detected in this system. If turbulence is responsible for the radio emission, we argue that it must develop before the core passage. A comparison of double relic plus halo system with cosmological simulations allows a simultaneous estimate of the acceleration efficiencies at shocks (to produce relics) and of turbulence (to produce the halo).

Key words: galaxies: clusters: intracluster medium; radiation mechanisms: non-thermal; radio continuum; magnetic fields; shock waves; turbulence; galaxies: clusters: individual: MACSJ1149.5+2223, MACSJ1752.0+4440, MACSJ0553.4-3342, MACSJ1731.6+2252.

1 INTRODUCTION

A fraction of galaxy clusters host diffuse radio emission, that is not connected to any of the cluster radiogalaxies. These radio sources are classified as radio halos and radio relics, depending on their location and morphology. In all these sources relativistic particles need to be (re)accelerated in order to produce the observed radio emission, even though the underlying physical mechanisms

are likely to be different. Radio halos permeate the central Mpc of galaxy clusters, and in some cases the radio emission roughly follows the X-ray emission from the thermal gas (see review by Ferrari et al. 2008, and references therein). Radio halos are characterized by a steep radio spectrum,¹ with $\alpha \geq 1.2$, and their power at 1.4 GHz correlates with the X-ray luminosity of the host cluster (Liang et al. 2000; Giovannini et al. 2009). The origin of radio

* E-mail: a.bonafede@jacobs-university.de

¹ We define here the spectrum as $S(\nu) \propto \nu^{-\alpha}$.

halos is still unknown, although a clear connection between the presence of a radio halo and the merging state of the host cluster is present (Buote 2001; Cassano et al. 2010; Brown et al. 2011b; Basu 2012). The models proposed so far can be divided into two classes: “hadronic models” (e.g. Dennison 1980; Keshet & Loeb 2010; Enßlin et al. 2011) and “re-acceleration models”. It was recently shown that hadronic models fail to reproduce the observed radio emission of the Coma cluster, once the upper limits by FERMI and the magnetic field estimate from Faraday Rotation Measures are combined (Donnert et al. 2010). Recent LOFAR radio observations of the cluster Abell 2256 have shown that the spectral flattening predicted at low frequencies by re-acceleration models are not observed (van Weeren et al. 2012b). Hence, the question about the origin of radio halos is still open, and it is likely that more complex scenarios have to be considered.

Radio relics are irregularly shaped radio sources, located at the outskirts of galaxy clusters. They usually have an arc-like structure, and are found to be polarized at 10 - 80% level (see review by Brügger et al. 2011, and references therein). Like radio halos, radio relics are characterized by a steep spectrum and a weak surface brightness at 20 cm that makes their detection difficult. Their origin is still unclear, but there is a common consensus that they are related to merger shocks. A merging shock could accelerate particles via Diffusive Shock Acceleration (DSA), and amplify the magnetic field strength in the shock region, hence producing radio synchrotron emission (e.g. Enßlin et al. 1998; Iapichino & Brügger 2012). Some clusters show a relic and a radio halo, like the Coma cluster (Giovannini et al. 1993), others, such as Abell 115 only host a single relic (Govoni et al. 2001), a few objects have been found where double relics are present (e.g. Abell 1240 and Abell 2345 Bonafede et al. 2009b). Finally, in a couple of objects, both double relics and a radio halo have been found (e.g. CIZA J2242.8+5301 van Weeren et al. 2010). The combinations with which halos and relics are found, and the number of these objects itself, are likely to be affected by detection limits of current instruments. In the last years, efforts have been made from both observational and theoretical sides to better understand the properties of radio relics. From a theoretical point of view, the properties of merging shocks, and the acceleration mechanism required to explain the radio emission, have been investigated in several works (Pfrommer et al. 2006; Hoefl & Brügger 2007; Battaglia et al. 2009; Vazza et al. 2009b, 2010; Skillman et al. 2011; Kang & Ryu 2011; Nuza et al. 2012; Vazza et al. 2012b; Iapichino & Brügger 2012). Recently, Nuza et al. (2012) have used hydrodynamic simulations to predict the number of observable relics as a function of the redshift. They find that either more relics with $z > 0.3$ should be found than known to date (only a couple have been observed so far), or that the ratio B/n_e of the magnetic field B over the thermal gas density, n_e , changes with z . The “lack” of relics at $z > 0.3$ can be however due to the lack of deep radio observations of distant galaxy clusters. Investigating the properties of galaxy clusters in this redshift range would hence provide information on the physics of the ICM itself. So far, the properties of radio halos and relics have been mainly studied in galaxy clusters at low redshift ($z < 0.3$). Giovannini et al. (2009) have analyzed the radio emission from a sample of galaxy clusters at $z < 0.2$, finding that at the NVSS detection limit, the percentage of galaxy clusters with diffuse sources is in the range 6-9% in clusters with X-ray luminosity $L_x > 10^{44}$ erg s⁻¹, and grows to ~40% when only clusters with $L_x > 10^{45}$ erg s⁻¹ are considered. Venturi et al. (2008) have searched for the presence of radio halos in a complete sample of X-ray luminous galaxy clusters, finding that the fraction of clusters with a radio halo is ~30% in the redshift

range 0.2 - 0.4 (with most of the objects having $z \leq 0.3$) increasing up to ~40% when clusters with $L_x > 8 \cdot 10^{44}$ erg s⁻¹ are considered. The aim of the present work is to extend the sample of diffuse radio sources to $z > 0.3$, the epoch when massive clusters formed. X-ray selected samples compiled from ROSAT data, such as REFLEX (Böhringer et al. 2004) and eBCS (Ebeling et al. 2000) have probed the radio properties of galaxy clusters in the local Universe (e.g. Venturi et al. 2008; Giovannini et al. 2009). At higher redshifts the MACS project has compiled the first large X-ray selected sample of clusters that are both X-ray luminous and distant (Ebeling et al. 2001). It consists of 128 clusters at $z > 0.3$. The MACS catalogs of Ebeling et al. (2007, 2010) comprise all clusters at $z > 0.3$ with a nominal X-ray flux larger than $2 \cdot 10^{-12}$ erg s⁻¹ cm⁻² (0.1–2.4 keV) in the ROSAT Bright sources catalog (Voges et al. 1999), and 12 clusters at $z > 0.5$ down to an X-ray flux limit of 1×10^{-12} erg s⁻¹ cm⁻². A third MACS subsample was recently published by Mann & Ebeling (2012).

We have inspected the archival Chandra/XMM-Newton data of the clusters contained in the MACS catalogs, and we have selected those that show a disturbed X-ray morphology. To start with, we have observed four promising candidates that show hints of diffuse emission from the NVSS (Condon et al. 1998). However, there are further candidates for diffuse emission in the MACS sample that will be followed up in future work.

The paper is organized as follows: The observations and the data reduction are described in Sec. 2, followed by the results in Sec. 3. We discuss our results in Sec. 4, and compare our observations with mock radio images obtained with cosmological simulations. In Sec. 5, we present new correlations for the radio halos and double-relic systems. Finally, we conclude in Sec. 6.

Throughout this paper we assume a concordance cosmological model Λ CDM, with $H_0 = 72$ km s⁻¹ Mpc⁻¹, $\Omega_M = 0.27$, and $\Omega_\Lambda = 0.73$.

2 RADIO OBSERVATIONS

2.1 GMRT observations and data reduction

The observations were carried out at the Giant Metrewave Radio Telescope (GMRT) during June - August 2010. We chose to perform the observations at 323 MHz, as this frequency provides the best compromise between sensitivity, resolution, and good sampling of the short baselines. High resolution is crucial, since the emission from discrete sources needs to be separated from the halo/relic emission. A good coverage of the short spacings is also required to image the diffuse emission. One Mpc corresponds to ~3' and 4' at redshift 0.5 and 0.3 respectively, much smaller than the largest visible structure of the GMRT at 323 MHz (32'). This ensures that radio emission with typical sizes of radio halos and relics can be imaged. Each cluster was observed for 6h, recording both RR and LL polarizations with 32 MHz bandwidth in 256 channels each. However, due to high wind speeds a considerable fraction of the observing time was lost in the June observations. We used 8 sec integration time for a more accurate removal of the Radio Frequency Interferences (RFI). To set the absolute flux density scale, the sources 3C286 and 3C48 (for MACSJ1752.0+4440), 3C48 (for MACSJ0553.4-3342), 3C147 and 3C286 (for MACSJ1149.5+2223), and 3C286 (for MACSJ1731.6+2252) were observed at the beginning/end of the observing run for 10-15 min. The flux density scale was set according to the Perley & Taylor (1999) extension of the Baars

Table 1. Observation details

Cluster	RA (J2000)	DEC (J2000)	z	Observation Date
MACSJ1149.5+2223	11 49 34.3	22 23 42	0.544 ^c	15-AUG-201
MACSJ1752.0+4440	17 52 01.5	44 40 46	0.366 ^b	27-JUN-2011
MACSJ0553.4–3342	05 53 26.7	-33 42 37	0.431 ^d	15-AUG-2010
MACSJ1731.6+2252	17 31 40.1	22 52 39	0.389 ^a	26-JUN-2011

Col. 1: cluster name; Col. 2 and 3: Right ascension and Declination (J2000) from RASS.

Col. 4: redshift (*a* : Ebeling et al. (2010), *b* : Edge et al. (2003), *c* : Ebeling et al. (2007), *d* : Mann & Ebeling (2012))

Col. 5: Observation date.

scale (Baars et al. 1977). Flux density calibrators were also used to correct the bandpass. To get a first calibration of the phases, we alternated in each observing run between the target source (40 min scan) and a phase-calibrator (5 min scan). As phase calibrators, we observed 1635+381, 0447-220, 1120+143, and 1609+266 for the clusters, MACSJ1752.0+4440, MACSJ0553.4-3342, MACSJ1149.5+2223, and MACSJ1731.6+2252 respectively.

The data were reduced using the NRAO Astronomical Image Processing Systems (AIPS) package. Data were visually inspected to identify and remove strong and low-level RFIs. Given the long initial scan on the flux density calibrator, and the relatively low observing frequency, we selected a few channels (3 to 5) and solved every 8 sec for the complex gains on the flux density calibrator sources before solving for the band response. This is done because the amplitude and phases can change over 10-15 min at this low frequency. Hence, such effects have to be taken out before the bandpass is computed over the whole calibrator scan (see also van Weeren et al. 2011c). After this initial calibration, we selected 10-15 channels free and/or cleaned from RFIs (usually 160-170) to normalize the bandpass. When 2 scans on the flux density calibrators were present, at the beginning and at the end of the observation, the bandpass solutions were computed separately for each scan, to check that the band response was stable. A time interpolation of the two was then applied to the data. After the bandpass calibration, the channels at the edges of the band were removed (usually the first and last 8 channels), and the remaining ones were averaged down to 48 channels. We did not average further in order to minimize the effects of bandwidth smearing. We then performed a more robust calibration of the flux density calibrator sources, this time including all the 48 channels, and solving for the whole scan, to get higher signal-to-noise solutions. Gains for the phase calibrators were then computed, and their flux densities were bootstrapped from the flux density calibrators. Solutions were interpolated and applied to the target sources. Several cycles of phase self-calibration have been done on the target source, followed by a final amplitude and phase self calibration run to refine the antenna gains.

In order to account for the effects of non-coplanar baselines, data were imaged using “3-dimensional” techniques: 40-45 facets were used in the cleaning procedure to cover an area equal to ~ 2 times the primary beam, with each facet being tangent to the celestial sphere at its centre. This ensures that side-lobes from distant sources are subtracted from the central field.

Different weighting schemes were applied to the data to obtain images at different resolution. Such weighting schemes are described in the section for individual clusters (Sec. 3). Finally, images were corrected for the primary beam attenuation. The uncertainty in the calibration of the absolute flux density scale is estimated to be $\sim 8\%$.

The errors reported on the flux density measurements are computed as

$$dS = \sqrt{(rms \times \sqrt{N_beam})^2 + (0.08 \times S)^2} \quad (1)$$

where rms is the rms noise of the image, N_beam is the number of independent beams in the region where the flux density, S , is measured.

2.2 VLA observations and data reduction

L-band observations of the cluster MACSJ1149.5+2223 have been retrieved from the VLA data archive. The observations were performed in the C array configuration. The source 3C286 was used as primary flux density calibrator and as an absolute reference for the electric-field vector polarization angle. The source 0842+185 was observed as phase calibrator, and together with the sources 0503+020 and 1125+261, they were used as parallactic angle calibrators. We performed standard calibration and imaging using the NRAO Astronomical Imaging Processing Systems (AIPS). Cycles of phase self-calibration were performed to refine antenna phase solutions on target sources, followed by a final amplitude and gain self-calibration cycle in order to remove minor residual gain variations. The uncertainty in the calibration of the absolute flux density scale is estimated to be $\sim 5\%$.

2.3 WSRT observations

The cluster MACSJ1752.0+4440 was observed with Westerbork Synthesis Radio Telescope at 13, 18, 21, and 25 cm, and the resulting images have been presented in van Weeren et al. (2012a). Here we use the 18 cm observation, that is 24 hour long, and provides the best imaging of the radio halo. We refer to van Weeren et al. (2012a) for details about the data calibration. The polarization was calibrated using 3C48 to remove instrumental polarization, and 3C286 as absolute reference for the electric vector polarization angle.

Total intensity, I, and Stokes parameter Q and U images have been obtained from VLA and WSRT images. Polarization intensity $P = \sqrt{U^2 + Q^2}$, Polarization angle $\Psi = \frac{1}{2} \arctan(U, Q)$ and fractional polarization $FPOL = P/I$ images were obtained from the I, Q and U images. Polarization intensity images have been corrected for a positive bias.

Table 2. X-ray properties

Cluster	L_X [r_{500}] [0.1 - 2.4 keV]	L_X [r_{500}] bolometric	kT keV
MACSJ1752.0+4440	$0.8 \cdot 10^{45b}$	-	6.7^b
MACSJ1149.5+2223	$1.4 \cdot 10^{45c}$	$5.1 \cdot 10^{45c}$	14.5^f
MACSJ0553.4-3342	$1.7 \cdot 10^{45d}$	$5.7 \cdot 10^{45d}$	13.1^e
MACSJ1731.6+2252	$0.8 \cdot 10^{45a}$	$2.5 \cdot 10^{45a}$	7.5^e

Col 1: cluster name; Col. 2: X ray Luminosity in the 0.1 - 2.4 keV Band; Col. 3: Bolometric X-ray Luminosity; Col. 4: Cluster temperature a : Ebeling et al. (2010), b : Edge et al. (2003), c : Ebeling et al. (2007), d : Mann & Ebeling (2012), e : Cavagnolo et al. (2008), f : Böhringer et al. (2000)

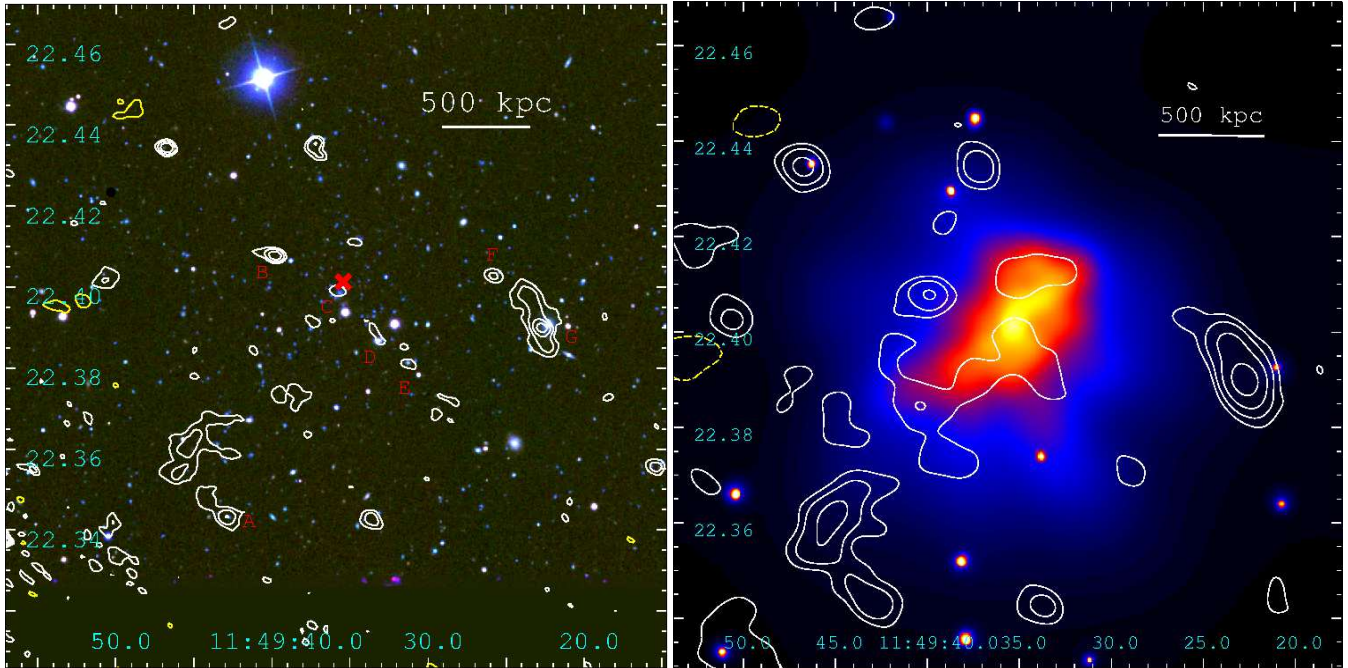


Figure 1. MACSJ1149.5+2223 *Left*: the colour image shows the emission (bands r, g and i) from the SDSS Data release 7. Contours show the radio emission at 323 MHz from the GMRT, obtained with Robust=0 weighting. The restoring beam is $11.5'' \times 7.8''$. The rms noise is $\sigma \sim 0.2$ mJy/beam. Contours start at 4σ and are spaced by powers of 2. The -4σ contour is displayed with dotted yellow lines. The red cross at the centre marks the position of the X-ray centre. Sources embedded in the relics' emission and within the cluster are marked by letters from A to F. *Right*: X-ray emission of the galaxy cluster as seen by Chandra ACIS-I detector, in the energy band 0.5-7 keV (Ebeling et al. 2007). Contours show the radio emission at 323 MHz from the GMRT obtained with a Gaussian taper of the long baselines and Robust=1 weighting. The restoring beam is $24.5'' \times 20.0''$. The rms noise is $\sigma \sim 0.4$ mJy/beam. Contours start at 3σ and are spaced by powers of 2. The -3σ contour is displayed with dotted yellow lines.

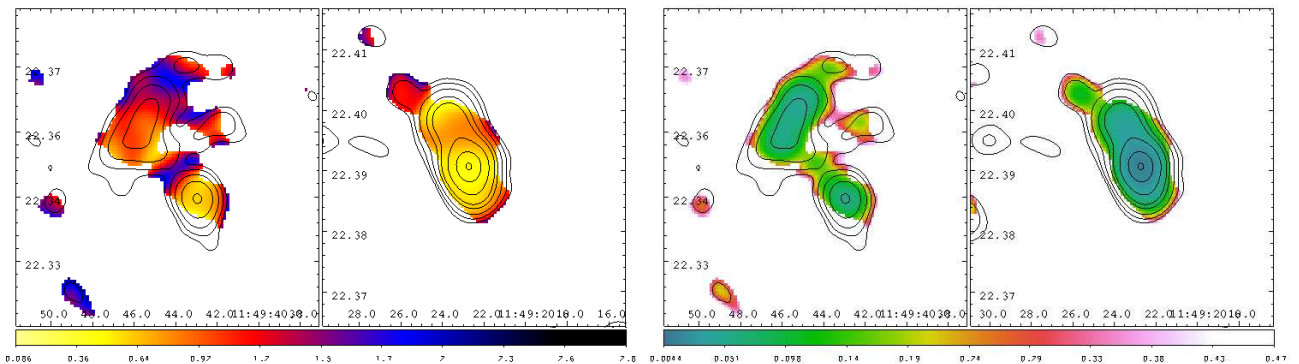


Figure 2. MACSJ1149.5+2223 Spectral index images and errors for the relics in MACSJ1149.5+2223. Contours start at 3σ and are spaced by powers of 2.

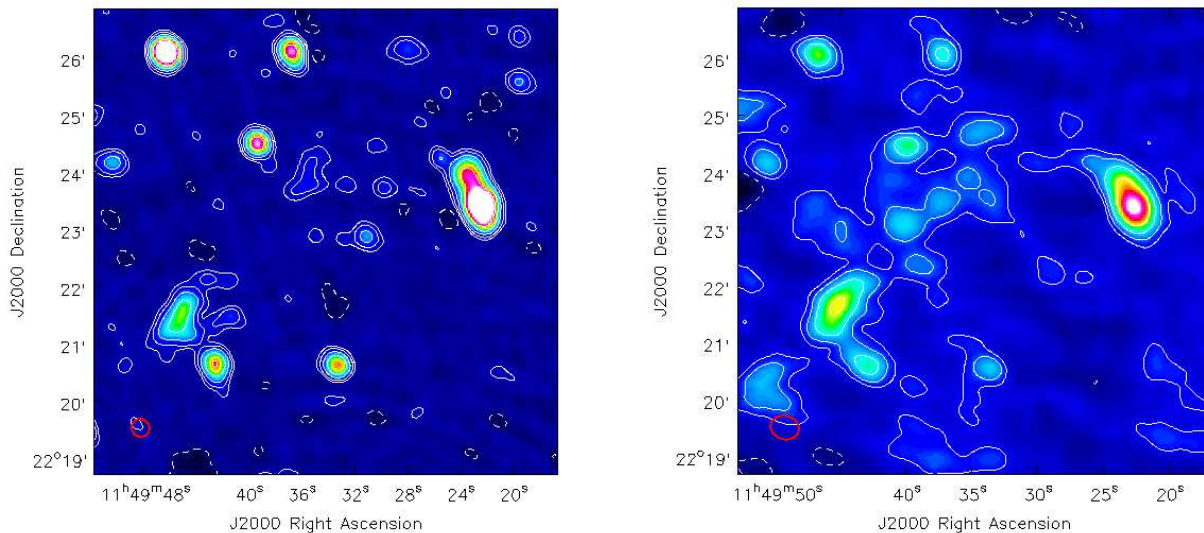


Figure 3. MACSJ1149.5+2223 Radio emission from the cluster at 1.4 GHz from VLA observations. The image is obtained with a Gaussian taper of the long baselines and Robust=1 weighting. The restoring beam is $\sim 20'' \times 20.0''$, the rms noise level is $30 \mu\text{Jy}/\text{beam}$. Contours start at 3σ and are spaced by powers of 2. The -3σ contour is displayed with dashed lines. Right: Low-resolution image at 323 MHz obtained with natural weighting. The beam is $\sim 30'' \times 25''$, The noise is $0.4 \text{ mJy}/\text{beam}$. Contours start at 2σ , the -2σ contour is displayed with dashed lines.

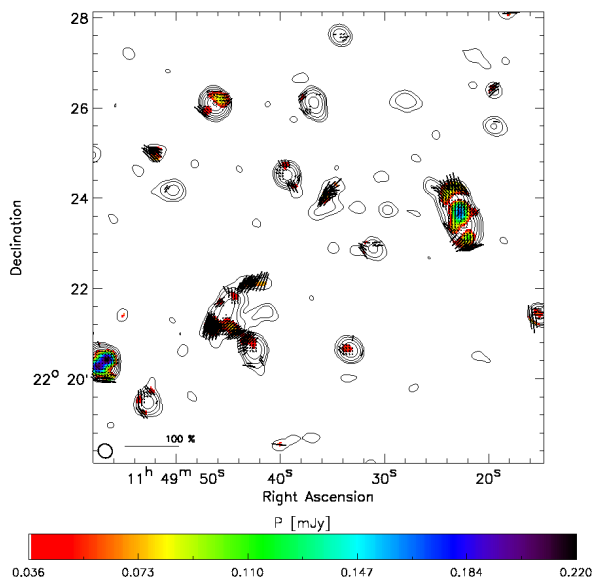


Figure 4. Polarized emission in MACSJ1149.5+2223. Colours display the polarization intensity, while the lines display the direction of the electric field vector de-rotated by the Galactic Faraday depth. The length of the vectors is proportional to the fractional polarization. For clarity, only one line every 3 pixels is plotted. Contours represent the VLA image obtained with natural weighting. The beam is $23'' \times 16''$, and is shown in red on the bottom left of the image. The noise is $15 \mu\text{Jy}/\text{beam}$. Contours start at 3σ and are spaced by powers of two.

3 RESULTS

3.1 MACSJ1149.5+2223

The cluster MACSJ1149.5+2223 was observed with the Advanced Camera for Surveys on board HST as part of a programme targeting

all MACS clusters at $z > 0.5$ (Ebeling et al. 2007). A strong lensing analysis by Smith et al. (2009) identified seven multiple-image systems and found the cluster to contain at least four large-scale mass concentrations, making MACSJ1149.5+2223 one of the most complex cluster lenses known to date. The contours of the luminous density, mass density, and X-ray surface brightness, as derived from Chandra observations (Ebeling et al. 2007), show a net elongation toward the SE-NW direction. These observations have been used to place constraints on the mass and structure of the cluster. The fiducial model contains the main cluster halo plus three group-scale halos. Ebeling et al. (2007) derived a total mass $M(\leq 500 \text{ kpc}) = (6.7 \pm 0.4) \times 10^{14} M_{\odot}$.

In the NVSS image, a radio source is located $\sim 130''$ SE from the cluster X-ray centre. This source is not detected in the FIRST survey (Becker et al. 1995) because it is either resolved out (i.e. $\geq 2'$), or below the sensitivity limit. Another source is located at $\sim 3.7'$ West from the cluster centre. It is detected in both FIRST and NVSS. We inspected the optical image of the cluster from the SDSS data release 7 (see Fig. 1). There is an optical counterpart associated with the radio source, located at $z=0.174$ (McMahon et al. 2002). The radio emission at 323 MHz is shown in Fig. 1. Two radio sources are located at $\sim 3'$ and $3.7'$ from the cluster X-ray centre, in SW and SE directions, respectively. Their extent is $\sim 2'$ and $2.2'$, which corresponds to 760 and 820 kpc at the cluster’s redshift. We classify these sources as peripheral radio relics, or radio “gischt”, because of their location and morphology. We note that there is a foreground radio-galaxy projected onto the W-relic. Nonetheless, the morphology of its emission and the fact that no jets/hot-spots are visible in the higher-resolution image from FIRST indicate that the diffuse radio emission is likely not due to the radio galaxy but originates from the ICM. We also note that further emission from the W-relic is present with lower significance (see Fig. 3, right panel). Although deeper observations would be required to definitely rule out an AGN origin for this emission, we classify this source as a relic. The two relics are clearly visible in the high-

resolution image, obtained with Robust=0 weighting (Fig. 1, left panel). The flux density of the discrete radio sources - labeled by letters in Fig. 1 - are reported in Table 4. In order to enhance the diffuse emission we have imaged the dataset with a different weighting scheme (Robust=1 and uv-taper of the long baselines). The final image is shown in the right panel of Fig. 1. Further diffuse emission is visible between the two relics which appears to be a radio halo as it follows approximately the X-ray brightness of the cluster. The flux density of the relics and of the candidate halo were computed from this image after subtracting the flux density of the sources as measured from the higher resolution image. To check the consistency of this approach, we have selected the emission of the radio galaxies embedded in the cluster's emission, and then subtracted the corresponding visibilities in the Fourier plane, and re-imaged the dataset with a different weighting scheme (Robust=1 and uv-taper of the long baselines). The two approaches give consistent results.

The VLA 1.4 GHz images of MACSJ1149.5+2223 are shown in Fig. 3. We imaged the dataset with Robust=0 weighting, to isolate the emission from the discrete radio galaxies, and with natural weighting to image the diffuse emission. The two relics are detected at 1.4 GHz. However, due to the poorer sampling of the inner uv-plane in comparison with GMRT observations, their emission is not as well recovered as in the 323 MHz image. The candidate halo is barely visible in the 1.4 GHz image. Details about the relics and the halo are reported in Table 3.

3.1.1 A spectral index study of the radio relics

Two radio relics are detected in this cluster at both 323 MHz and 1.4 GHz. The relics are located at the edges of the X-ray emission. The major axes of the relics are oriented perpendicular to the cluster's X-ray elongation, that is likely tracing the main merger axis of this complex system. However, the relic positions appear to be misaligned with the main merger axis, which is unique in double relics observed so far. This peculiar feature is not reproduced by simple simulations of binary mergers. We argue that it could be a sign of additional mergers.

In order to derive the integrated spectral indices of the relics' emission, we computed the radio brightness in the area where relics are above the 3σ level in both VLA and GMRT images. This cut is set by the VLA image, and thus the resulting spectral indices will be representative of the flatter spectra contributing to the relic emission. The integrated spectral indices are $\sim 0.75 \pm 0.08$ and $\sim 1.15 \pm 0.08$ for the Western and Eastern relic, respectively. After imposing a common uv-range cut in the GMRT and VLA datasets, the two were reimagined using uniform weighting and a tapering of the long baselines. Thus we take into account the different sampling of the uv-plane resulting from observations performed with different arrays, at the cost of losing part of the diffuse emission that is better sampled in the inner uv-plane of the GMRT observations. Both images were convolved to the same restoring beam of $20''$. The VLA and GMRT absolute position differ by each other by few arcsec. The geometry itself is distorted, so that there is not a single shift in RA or DEC, or a rotation of the coordinates, that is able to compensate for that. This is most likely caused by the self-calibration process in which the absolute position of the sources is lost. This affects particularly the GMRT observations since ionospheric effects can cause a shift in the absolute positions of the sources. We have then shifted the VLA map to fix the positions of sources A (for the Eastern relic) and F-G (for the Western relic) separately. The shifts required to match the position of the sources were $6''$ in RA and $2''$

in DEC for the Eastern relic, and $4''$ in both RA and DEC for the Western relic, respectively. Only pixels above 2σ in both images were considered for the spectral index map. Furthermore, pixels in the spectral index map with a signal-to-noise ratio smaller than 3 were blanked in the final spectral index image.

The resulting spectral-index maps are displayed in Fig. 2 together with the spectral index error maps. In the Eastern relic, the spectral index distribution shows flat values in the outer Eastern region ($\alpha \sim 0.6$) and steepens toward the North-West, up to $\alpha \sim 1.8$. The spectral index over the Western relic is more uniform, with values going from $\alpha \sim 0.7$ to ~ 1.1 , and no trend is detected towards the cluster centre.

A steepening of the spectral index is expected in the case of outgoing merger shock waves, and observed in some relics (e.g. Bonafede et al. 2009b; van Weeren et al. 2010). In MACSJ1149.5+2223, we do not detect such a clear trend. However, in this case the dynamic state of the ICM is more complex since X-ray and lensing observations indicate the presence of several groups. Due to the poor match of the absolute and relative positions for the two datasets, any further discussion would be too speculative.

3.1.2 Polarization properties

From U and Q Stokes maps, the polarized intensity and polarization angle maps were produced. We then derived the fractional polarization map by dividing the polarized intensity by the total intensity map. Pixels with noise larger than 10% were blanked. The relics show a mean polarization of $\sim 5\%$. Due to the beam size, it is likely that beam-depolarization occurs, so that this value should be taken as a lower limit to the intrinsic polarization. We note that $20''$ corresponds to ~ 100 kpc at the cluster redshift. The Galactic contribution to the observed polarization was estimated using the reconstructed map of the Galactic Faraday sky (Oppermann et al. 2011). The Galactic Faraday Depth at the location of the cluster is 0.68 ± 4.45 rad m^{-2} . The polarization vectors have been rotated accordingly. At such large distances from the cluster centre, the Rotation caused by the ICM is likely not significant, hence we assume that once the vectors are rotated by the Galactic FR, the result is the intrinsic polarization of the sources. The polarization image is shown in Fig. 4. The orientation of the vectors corresponds to the direction of the electric field vectors. In both relics, the magnetic field orientation is roughly aligned with the relics' main axis. as found in some of the relics observed so far (e.g. Bonafede et al. 2009b; van Weeren et al. 2010), and in agreements with theoretical expectations.

3.1.3 The radio halo

The GMRT 323 MHz image shows low-brightness emission in the cluster centre, covering the region in between the two relics. The brightest part of this emission is detected at 3σ , although we find indication of a larger and more extended emission with a lower significance (2σ above the noise level). To enhance the diffuse emission, in Fig. 3 we display a GMRT image obtained with natural weighting, and overlay the first contour at 2σ level. The shape of the radio emission roughly resembles the X-ray brightness distribution of the cluster (Fig. 1).

The radio halo is barely visible in the VLA 1.4 GHz image, probably because of the poorer sampling of the shortest baselines. Nonetheless, positive residuals are visible in this image as well.

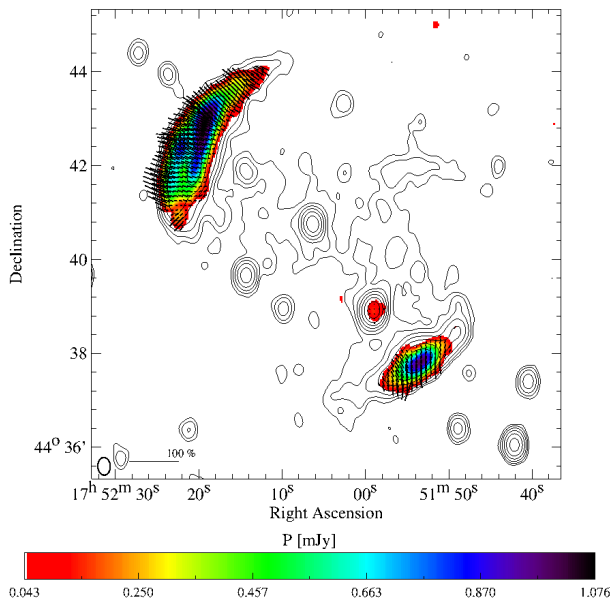


Figure 7. MACSJ1752.0+4440 polarized emission. Colours display the polarization intensity, while lines display the direction of the E vector de-rotated by the Galactic Faraday depth. The lines are proportional to the fractional polarization. For display purposes, only one vector every 3 pixels is plotted. Contours are drawn from the WSRT image, obtained with natural weighting. The beam size is plotted in the bottom-left corner of the image. Contours start at 3σ and are spaced by powers of 2.

In order to give an estimate of the radio halo power and spectral index, we have integrated the radio-flux density in the VLA and GMRT images, in the area where the halo emission is detected at the 2σ level. The values are noted in Table 3. Based on these values, the spectral index of the radio halo is $\alpha = 2.1 \pm 0.3$. The spectral index value has to be considered a lower limit to the real spectral index since only the brightest knots are detected in the VLA map. The errors on the flux densities were computed using the formula in Eq. 1 assuming 10% errors on the flux density scale for both VLA and GMRT images, due to the lower significance of the detections. If we only consider the area where the radio halo is detected at 3σ in the GMRT image, we derive a similar value of $\alpha \sim 2.2 \pm 0.2$. If confirmed, this would be the halo with the steepest spectrum known so far, and one of the very few with $\alpha > 1.6$. Such steep spectrum halos indicate synchrotron aging, difficult to explain with hadronic models (Brunetti et al. 2008 and Dallacasa et al. 2009). However, we note that deeper observations at 323 MHz and a better uv-coverage at 1.4 GHz are required to confirm the steep spectral index.

3.2 MACSJ1752.0+4440

This is the only cluster among those presented here, that has not been observed with Chandra. The XMM-Newton image shows the cluster to be elongated in the SE-NW direction, indicative of an on-going merger in that direction. Edge et al. (2003) point out that it is a very promising candidate to host two radio relics, as seen from NVSS and WENSS radio images. Recently, van Weeren et al. (2012a) have confirmed the presence of such diffuse emission with

Westerbork observations.

Our GMRT observation confirms the presence of the two relics and of a low-brightness radio halo (Fig. 5). The relics have a similar extension and morphology at 323 MHz and 1.7 GHz, although 1.7 GHz observations show a larger extent for the SW relic. We consider the centre of the cluster to be the midpoint between the two brightest X-ray cores. The distance of the NE and SW relics from the cluster centre is approximately 1130 kpc and 910 kpc. Their main properties are listed in Table 3. A very extended radio halo is detected in-between the two relics. The emission of the radio halo at 323 MHz is more extended than at 1.7 GHz (van Weeren et al. 2012a). The total extent in the NW-SE direction seems wider at 323 MHz, although a region located in the NE part is only detected at 1.7 MHz. This indicates that particles with different spectra are involved in the radio halo emission and/or that the magnetic field strength is non-uniform. The radio emission follows the elongation of the X-ray emission with a rather flat brightness distribution. The halo is elongated along the NE-SW direction, with a fairly irregular morphology. It is worth noting that there is no clear correlation between radio and X-ray surface brightness in this cluster: the brightest parts of the X-ray emission do not correspond to the brightest radio emission. If we are observing the first major-merger encountered by the galaxy cluster through its life, this feature could be attributed to the less regular and symmetric atmosphere that characterizes the ICM at this stage. Details about the radio halo properties are listed in Table 3.

3.2.1 Spectral index analysis

Using WSRT data at 18 cm and the GMRT data, we derive the integrated spectral indices of the radio relics and of the halo. In order to compute the spectral indices, the flux densities have been computed in the area where both WSRT and GMRT images show emission above 3σ . For the relics this is not critical since their sizes are very similar at the two frequencies. However, the radio halo appears on average more extended at 323 MHz, but some regions in the North are visible only in the WSRT radio image. The spectral indices we derive are 1.21 ± 0.06 and 1.12 ± 0.07 for the NE and SW relic, respectively. The radio halo has a spectral index of 1.33 ± 0.07 .

WSRT 1.7 GHz and GMRT 323 MHz observations have been used to produce a spectral index image of the radio emission. The two datasets were re-imaged using the same UV-range, uniform weighting and a Gaussian uv-taper of the long baselines. This ensures that different samplings of the uv-plane, due to the different instruments, are properly taken into account. The downside is that the extended weak diffuse emission is partly lost. In particular, the radio halo has a uniform brightness at 323 MHz and a large angular size of $\sim 5.5'$ so that only the brightest knots are visible in the GMRT map. The spectral index image is shown in Fig. 6. Only pixels above 2σ in the individual images were considered for the spectral image, and furthermore, pixels with S/N ratio smaller than 3 were blanked out in the output image. The NW relic shows a clear steepening of the spectral index going from the cluster periphery toward the centre. Such a clear trend has been detected before only in the northern relic of CIZA2242.8+5301 (van Weeren et al. 2010). The spectral index values range from $\alpha \sim 0.6$ to $\alpha \sim 2.5$. The SW relic shows also a net gradient along the relics' main axis. The flattest part of the spectral index is not located at the edge of the relic emission, but more central, and coincide with the peak of the radio emission. This could suggest that the possible shock responsible for the relic origin is propagating oriented at a tiny angle toward the observer. If

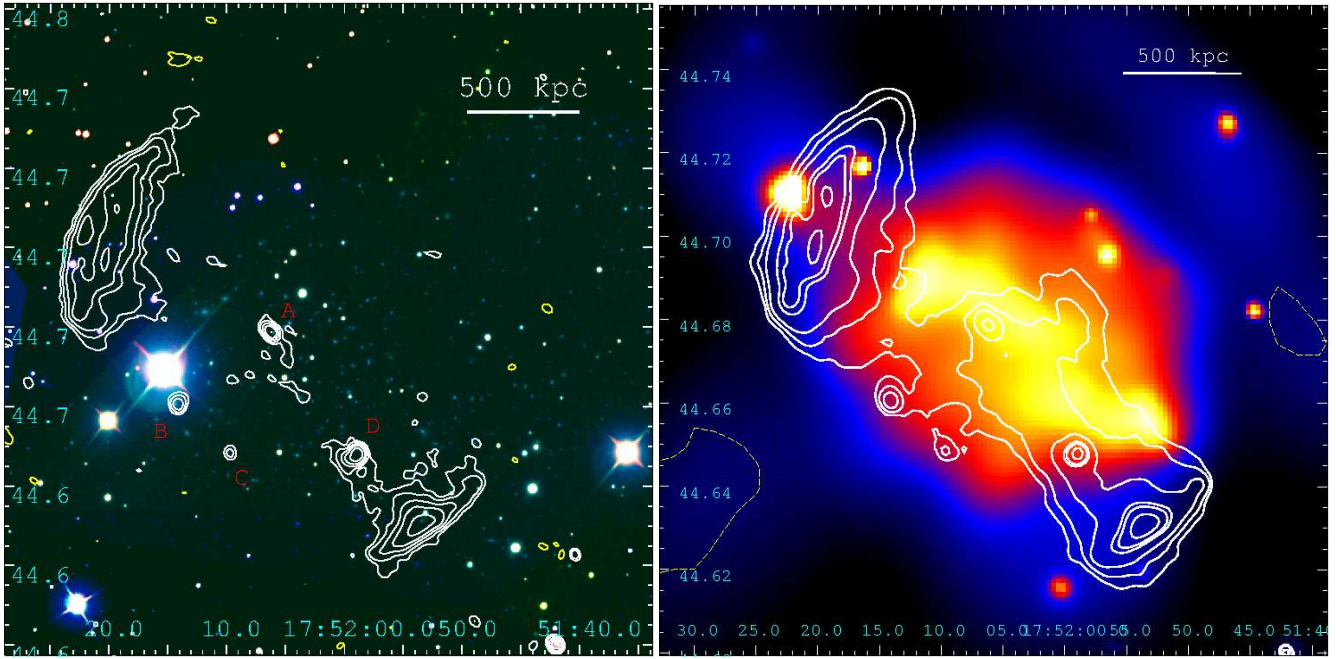


Figure 5. MACSJ1752.0+4440 *Left:* the colour image shows the emission (i, r and g band) from the SDSS data release 7. Contours show the radio emission at 323 MHz from the GMRT, obtained with Robust=0 weighting. The restoring beam is $9.9'' \times 8.0''$. The rms noise is $\sigma \sim 0.2$ mJy/beam. Contours start at 3σ and are spaced by powers of 2. The -3σ contour is displayed with dotted yellow lines. The red crosses at the centre mark the position of the X-ray peaks. *Right:* X-ray emission of the galaxy cluster as seen by *XMM-Newton* in the energy band 0.2-12 keV. Contours show the radio emission at 323 MHz from the GMRT obtained with natural weighting. The restoring beam is $13.7'' \times 10.2''$. The rms noise is $\sigma \sim 0.8$ mJy/beam. Contours start at 3σ . Given the uniform brightness of the diffuse emissions, contours here are plotted at [0.0025,0.003,0.004,0.008,0.01,0.0015,0.003] mJy/beam. The -3σ contour is displayed with dotted yellow lines.

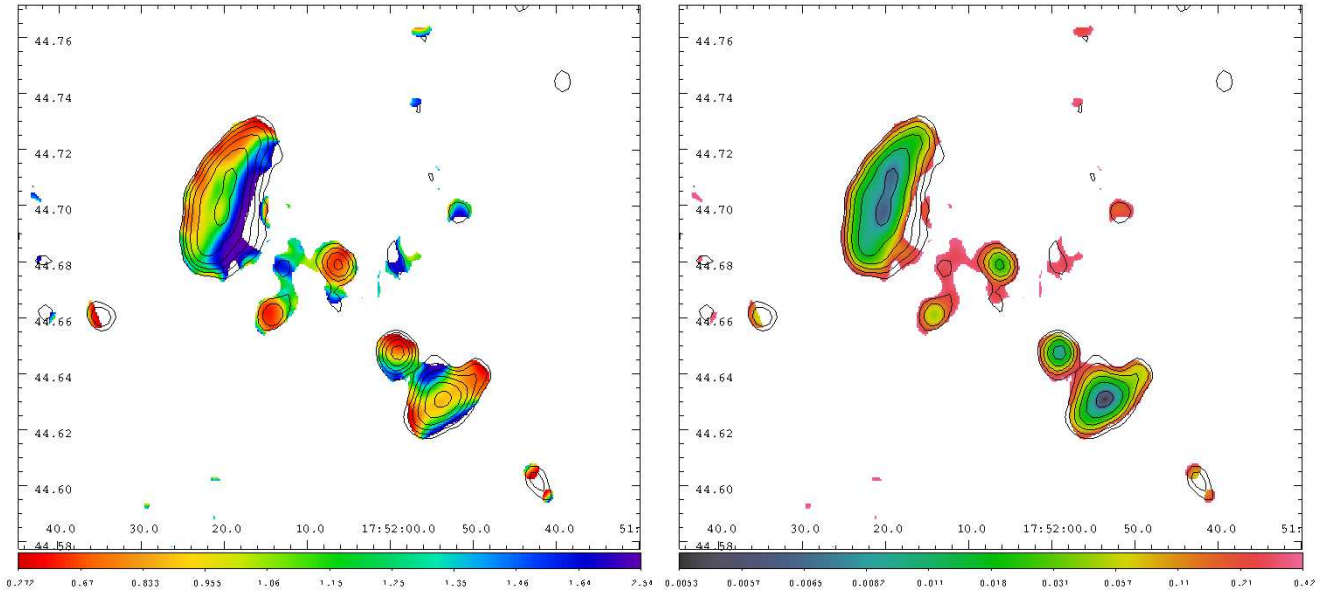


Figure 6. MACSJ1752.0+4440 Colours: spectral index (left) and errors (right). Contours are drawn from the GMRT image. Details about the imaging parameters are reported in Sec. 3.2.1. The beam is $\sim 24'' \times 10''$. The noise is 0.3 mJy/beam. Contours start at 3σ and are spaced by powers of 2.

that is the case, the freshly accelerated particles are seen in the foreground of the already aged ones. The spectral index values range from $\alpha \sim 0.8$ to $\alpha \sim 1.7$ towards the edges of the relic.

3.2.2 Polarization

WSRT observations provide polarization information for the cluster radio emission. From Stokes U and Q images we have derived the polarization intensity image, the image of the polarization angle and the fractional polarization map as explained in Sec. 3.1.

The Galactic Faraday rotation was corrected as explained in the same Section. MACSJ1752.0+4440 is at Galactic longitude 71° and latitude 29° . The galactic Faraday depth is estimated to be $37.65 \pm 11.15 \text{ rad m}^{-2}$ (Oppermann et al. 2011) and the polarization angles have to be rotated accordingly. The polarization image is displayed in Fig. 7. It shows that the NW relic is polarized on average at a 20% level, with values going up to 40%. The polarization is higher in the relics' external region, and decreases gradually towards the cluster centre. The SW relic is polarized at a 10% level, on average, with values up to 40% in the external region. The high level of polarization suggests an ordered magnetic field at the relic position. It is possible that turbulent motions developed after the shock passage contribute to randomize the magnetic field, hence reducing the observed polarized flux.

3.3 MACSJ0553.4-3342

MACSJ0553.4-3342 is a disturbed cluster, as evident from both optical and X-ray images (Mann & Ebeling 2012; Ebeling et al. 2010). According to Mann & Ebeling (2012) it is undergoing a binary head-on merger, and it is currently observed after the core passage. Two X-ray peaks, clearly visible in the image, are likely to be the cores of the two clusters. The X-ray isophotes show a net elongation in the EW direction (Fig. 8). From the analysis of Chandra data, Mann & Ebeling (2012) derive that the two clusters involved in the merger are likely to have the same mass, and from the separation between the two clusters, the authors conclude that the merger axis lies approximately in the plane of the sky.

In Fig. 8 the radio emission of the cluster is shown. We detect a $\sim 4'$ wide radio source, that is almost resolved out in the higher resolution image (Fig. 8, left panel). We classify such a source as radio halo. From optical radio overlays, we identify only one radiogalaxy in the region of the radio halo emission (labeled by letter A in Fig. 8, left panel), while the radio emission at the centre of the cluster corresponds to the brightest part of the radio halo. The radio halo shows a uniform brightness, and its emission is elongated toward the EW direction, following the gas distribution, as traced by the X-ray emission. One of the X-ray peaks coincides with a region of higher radio brightness. The flux density, power, and the Largest Linear Size (LLS) of the radio halo are noted in Table 3.

3.4 On the absence of radio relics in MACSJ0553.4-3342

We note that in this cluster, although we are likely to witness an energetic merger in the plane of the sky, no radio relic is detected. According to Poole et al. (2006), the X-ray luminosity of the cluster translates into a mass of $\sim 10^{15} M_\odot$. This estimate is robust against a possible uncertainty in the mass-ratio and impact-parameter of the merger. A binary head-on merger between clusters with this mass is expected to produce Mpc-sized shocks in the ICM. Moreover, the geometry of the merger, with the merger axis in the plane of the sky, should give the best orientation to detect the relic emission (e.g. Vazza et al. 2012b). The two clusters are likely to have the same mass (Mann & Ebeling 2012). The resulting Mach number of the merger shocks is expected to be low, since to first approximation the two clusters will fall into each other with virial velocities. We can roughly estimate how far a low Mach number shock could travel in the ICM under these conditions. Following Sarazin (1999), the relative impact velocity of two subclusters with Mass $\sim 10^{15} M_\odot$ at the distance of 1 virial radius is $\approx 2400 \text{ km s}^{-1}$. The distance between the two gas cores is now $\sim 200 \text{ kpc}$. The brightest galaxies,

that can be used as tracers for the Dark Matter (DM) components, is instead $\sim 500 \text{ kpc}$ (Mann & Ebeling 2012). Assuming that the infall velocity is constant, the two gas cores would take $\sim 0.08 \text{ Gyr}$ to achieve the observed separation. In this time, a shock wave with a Mach number $M \sim 2$ would travel a distance of $\sim 570 \text{ kpc}$, hence, a relic/shock wave should be well within the radio and X-ray fields of view. There are however some possibilities to maintain the correlation between relics and shock-wave: (i) the wave front is currently located along the merging axis, close to the clusters' cores. Such regions are already hot, and the resulting Mach number ≤ 1 . This situation could e.g. resemble the one in MACSJ0717+3745 (Bonafede et al. 2009a but see van Weeren et al. 2009c for a different interpretation). It is also possible that radio relics are actually present, but not visible because of the low contrast against the halo emission. Radio polarization information would resolve the issue. (ii) If the Mach number is low (i. e. $\leq 2-3$) DSA models predict a low electron-acceleration efficiency (Hoeft & Brüggén 2007), although low Mach number shocks have been observed to produce radio emission (e.g. Markevitch et al. 2005). (iii) At a redshift of 0.431 the magnetic field at the periphery of the ICM is lower than the equivalent Inverse Compton magnetic field ($B_{\text{ICM}} \sim 6.6 \mu\text{G}$), so that IC losses dominate over synchrotron losses, and no relic is visible. If this is the case, we should expect to detect only a few relics at similar redshifts, generated by high Mach number shock waves. DSA is the most simple mechanism that can power the radio emission in relics. Other less efficient mechanisms could be responsible for the relic emission, as e.g. the one proposed by Siejkowski et al. (2010). We note two recent works indicate that shock waves alone are not sufficient for powering the relic radio emission: Russell et al. (2011) detect two shock waves but no radio relic in the cluster Abell 2146. In order to explain the radio relic in Abell 754, Macario et al. (2011) claim that a direct acceleration of the electrons from the thermal pool to ultra-relativistic energies is problematic. Shock waves need to encounter a pre-existing population of relativistic electrons to produce the radio emission.

3.5 Time-scale for particle acceleration in the radio halo

Assuming that the merger axis is in the plane of the sky, as suggested by X-ray observations, we have derived that the collision between the two gas cores took place $\sim 0.08 \text{ Gyr}$ ago. The presence of a radio halo in this young-merger cluster can put constraints to the time-scale for acceleration processes. According to turbulent re-acceleration models, the cascade time of the largest turbulent eddies is of the order of 1 crossing time. During this time, the diffusion and transport of the turbulent eddies may fill a large region, and give rise to radio emission throughout the whole cluster volume (Cassano & Brunetti 2005). In the case of MACSJ0553.4-3342, the crossing time for a region of 1.3 Mpc, over which the radio emission is detected, is $\sim 0.5 \text{ Gyr}$. If turbulence is injected when the cores pass each other, the time-scale is not sufficient for the turbulent process to re-accelerate the particles over such a large and uniform volume. We conclude that either the merger is not in the plane of the sky, contrary to what is suggested by X-ray observations, or the turbulence started to develop well in time before the core passage, for instance by smaller groups and sub-clumps accreting along the merger axis (Vazza et al. 2011a). Alternatively, the radio halo in this system cannot be explained by turbulent re-acceleration alone.

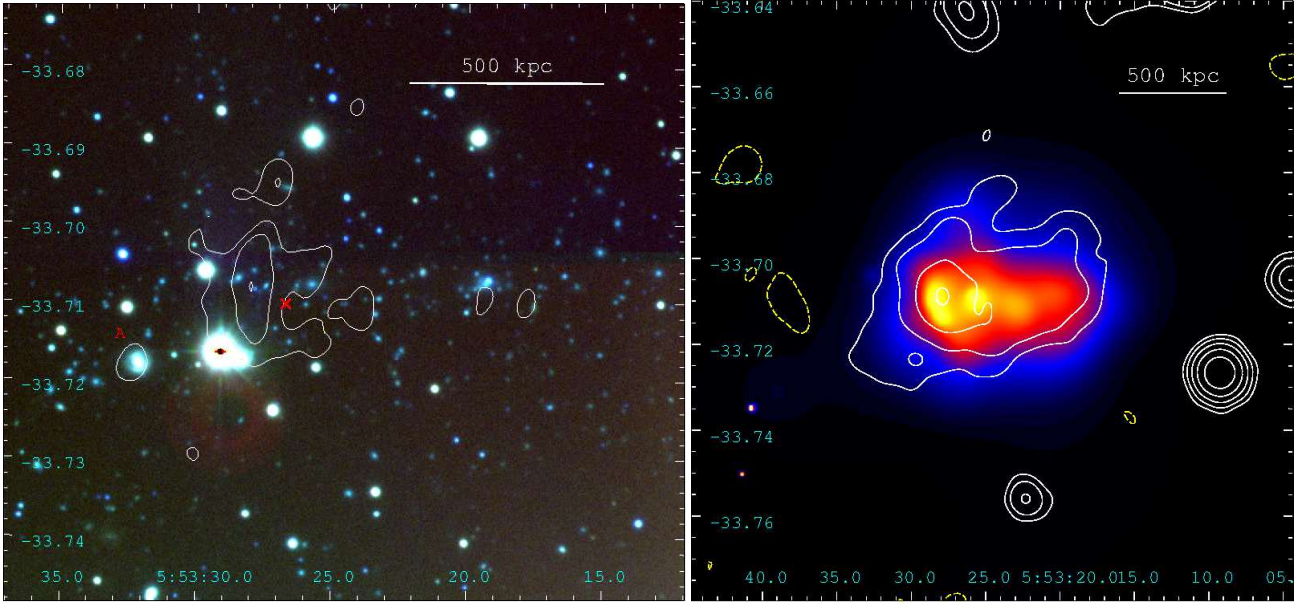


Figure 8. *MACSJ0553.4-3342* *Left:* the colour image shows the emission (v, r, and i bands) from the UH2.2m telescope (Mann & Ebeling 2012). Contours show the radio emission at 323 MHz from the GMRT, obtained with Robust=0 weighting. The restoring beam is $13.7'' \times 8.6''$. The rms noise is $\sigma \sim 0.14$ mJy/beam. Contours start at 3σ and are spaced by powers of 2. The -3σ contour is marked by a yellow line. The red cross at the centre marks the position of the X-ray centre. The source embedded in the halo emission is marked by letter A. *Right:* X-ray emission of the galaxy cluster as seen by *Chandra* ACIS-I detector, in the energy band 0.5-7 keV (Ebeling et al. 2007). Contours show the radio emission at 323 MHz from the GMRT obtained with a Gaussian taper of the long baselines and Robust=3 weighting. The restoring beam is $23.2'' \times 21.0''$. The rms noise is $\sigma \sim 0.25$ mJy/beam. Contours start at 3σ and are spaced by powers of 2. The -3σ contour is marked by a yellow line.

Table 3. Radio properties

Cluster	Source	freq MHz	S mJy	L $10^{25} \text{ W Hz}^{-1}$	LLS kpc	distance kpc
MACSJ1149.5+2223	W-Relic	323	17 ± 2	1.73 ± 0.1	760	1140
MACSJ1149.5+2223	E-Relic	323	23 ± 2	2.79 ± 0.2	820	1390
MACSJ1149.5+2223 ^a	Halo (?)	323	29 ± 4	4.77 ± 0.3	1300	-
MACSJ1149.5+2223	W-Relic	1450	5.6 ± 0.3	0.56 ± 0.03	730	1100
MACSJ1149.5+2223	E-Relic	1450	4.1 ± 0.2	0.50 ± 0.02	860	1380
MACSJ1149.5+2223 ^a	Halo(?)	1450	$\sim 1.2 \pm 0.5$	$\sim 0.19 \pm 0.09$	-	-
MACSJ1752.0+4440	NE-Relic	323	410 ± 33	19 ± 2	1130	1300
MACSJ1752.0+4440	SW-Relic	323	163 ± 13	7.3 ± 0.6	910	800
MACSJ1752.0+4440	Halo	323	164 ± 13	7.8 ± 0.6	1650	-
MACSJ0553.4-3342	Halo	323	62 ± 5	$4.4 \pm 0.4^*$	1300	-

Col 1: Cluster name; Col. 2: type or radio source in the cluster: H= radio halo, R= radio relic;

Col. 3 reference frequency for the table entries; Col 4 and 4: Radio flux density and radio power;

Col 6: Largest Linear Scale of the diffuse emission; Col. 7: Projected distance from the cluster centre;

^a = flux density is computed above 2σ level. Errors are computed assuming 10% errors on the absolute flux density. * = we assume $\alpha = 1.3$ for the k-correction.

3.6 MACSJ1731.6+2252

MACSJ1731.6+2252 was classified as an active merger by Mann & Ebeling (2012) in a study based on a comparison of *Chandra* and optical images. The authors suggest that the main cluster, which shows no significant optical-X-ray offset, has just undergone

a merger with a much less massive subcluster. We should be seeing the system after the core passage. The lack of a significant offset between optical and X-ray components might suggest a collision at large impact parameter, or a significant inclination of the merger axis with respect to the plane of the sky (Mann & Ebeling 2012). The *Chandra* image and the optical DSS image are shown in Fig. 9.

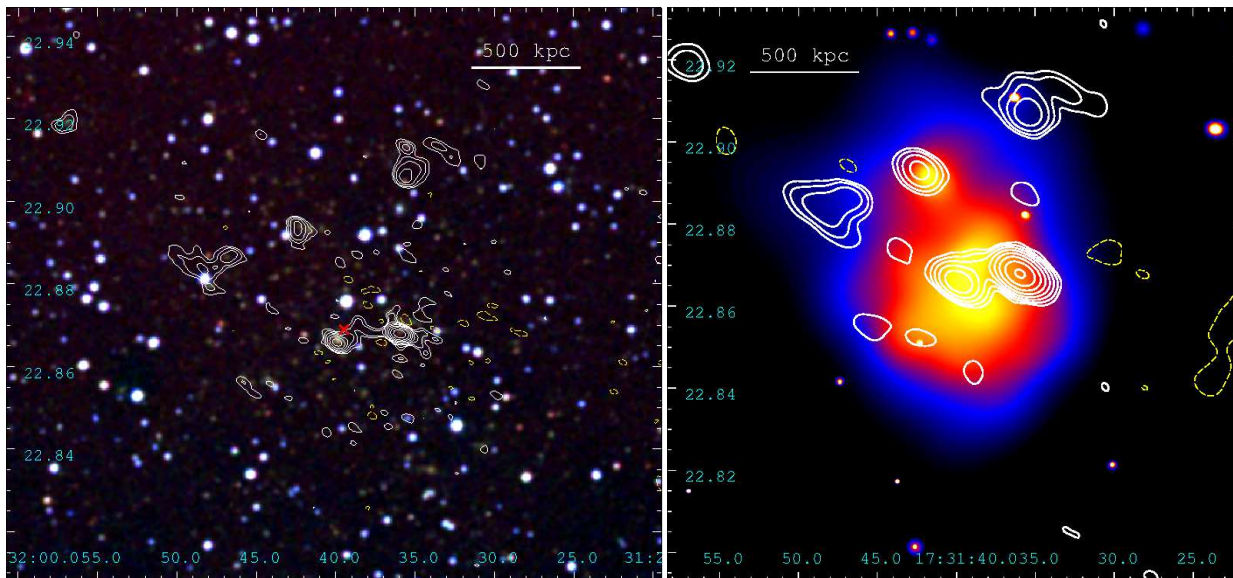


Figure 9. MACSJ1731.6+2252 *Left*: the colour image shows the emission (infra-red, red and blue) from the second Digitized Sky Survey (DSS II). Contours show the radio emission at 323 MHz from the GMRT, obtained with Robust=0 weighting. The restoring beam is $10.6'' \times 6.6''$. The rms noise is $\sigma \sim 0.3$ mJy/beam. Contours start at 4σ and are spaced by powers of 2. The -4σ contour is displayed with dotted yellow lines. The red cross at the centre marks the position of the X-ray centre. *Right*: X-ray emission of the galaxy cluster as seen by *Chandra* ACIS-I detector, in the energy band 0.5-7 keV (Ebeling et al. 2010). Contours show the radio emission at 323 MHz from the GMRT obtained with a Gaussian taper of the longer baselines and Robust=1 weighting. The restoring beam is $26'' \times 17''$. The rms noise is $\sigma \sim 0.5$ mJy/beam. Contours start at 4σ and are spaced by powers of 2. The -4σ contour is displayed with dotted yellow lines.

More details about the X-ray properties of the cluster are listed in Table 2.

The radio emission of the cluster is shown in Fig. 9. The hint of diffuse radio emission, visible in the NVSS image, results from the blending of the discrete radio sources. MACSJ1731.6+2252 is an example for a cluster that shows no diffuse radio emission, although it is in a clear merging state. In the re-acceleration model, this can be explained if the merger is minor, as the optical and X-ray data suggest (Mann & Ebeling 2012). In this case, the energy released into the ICM may not have been sufficient to power the radio emission at the sensitivity level of these observations. Observations at lower frequencies may detect the emission from the less energetic particles. Alternatively, not enough time may have elapsed to transfer energy from the large-scale turbulence to the relativistic particles. According to Cassano & Brunetti (2005), the cascade time of the largest eddies of MHD turbulence to the acceleration scale is of the order of ~ 1 Gyr (see however Sec. 3.4).

4 DISCUSSION

4.1 Shock properties from radio emission

If relics originate from shock acceleration, the radio properties of the observed emission reflect the properties of the shock wave. In particular, in the regime of DSA, the Mach number, M , of the shock is related to the observed radio spectral index through (Blandford & Eichler 1987)

$$\alpha_i = -\frac{1}{2} + \frac{M^2 + 1}{M^2 - 1} \quad (2)$$

where α_i refers to the injection spectral index. If we assume that particles are accelerated in regions with flatter spectra, we get $\alpha_i \sim 0.6$ and 0.8 for the NE and SW relics of MACSJ1752.0+4440,

respectively. These α_i correspond to $M \sim 4.6$ and 2.8 for the NE and SW relic respectively. In the cluster MACSJ1149.5+2223 the flattest values of the spectral index are 0.7 and 0.6 for the E and W relic respectively, corresponding to $M \sim 3.3$, and $M \sim 4.6$ for the E and W relic respectively. According to cosmological simulations, shocks with these Mach numbers are very rare event (Vazza et al. 2011b; Skillman et al. 2011; Vazza et al. 2012a). Such simulations also show that the Mach number can vary across the shock front. In these cases, the Mach numbers derived from the radio spectral index would be biased to higher values, since the synchrotron luminosity strongly increases with Mach number. It would not be surprising, then, if the Mach numbers derived from the gas properties were slightly lower than those inferred from the radio spectral indices.

4.2 Comparison with numerical simulations

In this section we compare our observations with mock radio and X-ray images obtained from cosmological simulations (Vazza et al. 2010). Cosmological simulations of large volumes of the Universe routinely provide a variety of merger configurations for evolving galaxy clusters, which can be used to guide the physical interpretation of observed radio and X-ray features (e.g. Donnert et al. 2010; Solovyeva et al. 2008, for recent comparison between cosmological simulations and observations of particular objects.) We tried to find constraints to our observations in a sample of clusters produced in high-resolution cosmological simulations (Vazza et al. 2010, 2011a). These simulations were performed using the ENZO code (e.g. Collins et al. 2010, and references therein.) We inspected the projected X-ray images (in the 0.5-2 keV band) of each object along many projections, for ~ 200 simulated outputs in the range $0 \leq z \leq 1$. Based on the morphology of the images, we found one case which was very similar to the X-ray data of

Table 4. Flux density of the radio sources embedded in the diffuse emission

Source	flux 323MHz mJy	flux 1.4 GHz mJy
MACSJ1149.5+2223 A	5.5±0.4	1.51±0.09
MACSJ1149.5+2223 B	6.6±0.5	2.08±0.1
MACSJ1149.5+2223 C	1.8±0.1	-
MACSJ1149.5+2223 D	1.09±0.09	-
MACSJ1149.5+2223 E	1.3±0.1	0.52±0.03
MACSJ1149.5+2223 F	2.9±0.2	0.37±0.02
MACSJ1149.5+2223 G	12.5±1	8.2±0.5

Source	flux 323MHz mJy	flux 1.7 GHz mJy
MACSJ1752.0+4440 A	12.2±0.9	3.3 ±0.2
MACSJ1752.0+4440 B	6.3±0.5	1.5 ±0.1
MACSJ1752.0+4440 C	1.8±0.1	3.4±0.2
MACSJ1752.0+4440 D	31.7±2.5	7.2±0.4
MACSJ1752.0+4440 E	-	0.37±0.02
MACSJ1752.0+4440 F	-	0.17 ±0.07

Source	flux 323MHz mJy	
MACSJ0553.4-3342 A	2.0 ±0.2	-

MACSJ1752.0+4440. We then computed the structure of turbulent motions and shock waves in this system, and estimated the kinetic energy flux dissipated by turbulent motions and shock waves, studying their possible link to the observed large-scale radio emission. Figure 10 shows the projected X-ray images of this cluster merger. The top left panel shows the X-ray and radio emission of a merging cluster at $z = 0$, about $\sim 0.8 - 1$ Gyr after the collision of the cores. The total virial mass of the system at this redshift is $\approx 0.65 \cdot 10^{15} M_{\odot}$. In post-processing, we measured the strength of shocks and turbulent motions at high resolution. Thus we obtain an estimate of the power that shocks and turbulent motions can provide to particle acceleration at the epoch of the observation. Shock waves are detected with an algorithm based on velocity jumps and divergence as well as the temperature jump. With this technique we can assign a Mach-number to each shocked cell in the simulation, and compute the kinetic energy flux across each shocked surface. For detailed information on this algorithm we refer the reader to Vazza et al. (2009a). Turbulent motions are extracted from the velocity field with an algorithm recently presented in Vazza et al. (2012c). This algorithm recursively analyzes the local mean velocity field around each simulated cell, and reconstructs the maximum correlation scale of turbulent motions across the simulated volume. In order to estimate the radio emission from shock acceleration (e.g. Hoeft & Brüggén 2007) and turbulent re-acceleration (e.g. Brunetti et al. 2001), we followed the simple approach of producing projected maps of energy flux from relativistic electrons accelerated by shocks and turbulence: The kinetic flux through the shock is $\Phi_{\text{shock}} = \int \rho v_s^3 dx^2 / 2$ (where ρ is the up-stream gas density, v_s is the shock velocity and dx is the cell size), and $\Phi_{\text{turb}} = \int \rho \sigma_t^3 dx^3 / (2 \cdot l_t)$ (where σ_t is the local turbulent velocity dispersion, and l_t is local outer scale of turbulence) for the turbulent

kinetic energy flux.

At a given frequency, we assume that energy is converted from shocks with an efficiency A_s such that $P_{\text{relic}} \sim A_s \Phi_{\text{shock}}$, and for turbulence with an efficiency A_t such that $P_{\text{halo}} \sim A_t \Phi_{\text{turb}}$. Various physical processes can set these conversion factors, such as DSA, particle-wave couplings, and damping with thermal plasma. The local magnetic field is also folded into these conversion factors. In addition, inefficient turbulent re-acceleration may cause a high time-variability of particle spectra (e.g. Brunetti et al. 2001). Here we apply these simple recipes to estimate the morphologies and intensities of radio power from the simulated cluster. To start with, we assumed a constant magnetic field strength $B = 1 \mu\text{G}$ across the whole simulated volume, and tuned the efficiency for conversion of kinetic energy into synchrotron emission at shocks, A_s to fit the observed power and morphology of the NE relic ($\sim 2 \cdot 10^{26} \text{ erg s}^{-1} \text{ Hz}^{-1}$ at 325 MHz). The simulated NE relic (third panel in the top row of Fig.10) is produced by a shock with an average Mach number of $M \approx 4.5 - 5.5$, very similar to the value derived from the radio spectral index. The total radio power for this region is equal to the one of the NE relic in MACSJ1752.0+4440 if we impose $A_s \approx 10^{-5}$. For this rather strong shock, this value of A_s would imply an electron to proton acceleration efficiency in the range of $R_{e/p} \sim 10^{-3} - 10^{-4}$ (e.g. Hoeft & Brüggén 2007), in line with recent numerical results (e.g. Skillman et al. 2011; Nuza et al. 2012). We then varied A_t in the simulation to match the observed power and morphology of the central halo in MACSJ1752.0+4440. We find that the best match is achieved for $A_t \sim 0.05$. Typical values of the turbulent velocity measured in this region are of the order of $\sim 500 \text{ km s}^{-1}$ (while the bulk motions of the ICM in the "halo" region are of the order $\sim 1500-2000 \text{ km s}^{-1}$). We note that our estimate of A_t is different from the efficiency of turbulent acceleration, η assumed in theoretical models. Usually, the efficiency of turbulent (re)acceleration in theoretical models is scaled to the *pre-impact* kinetic energy of the two colliding clusters (e.g. Fujita et al. 2003; Cassano & Brunetti 2005), while in our simulations we compute the turbulent kinetic energy $\sim 0.8 - 1$ Gyr after the collision. Our estimate of A_t is consistent with a value of $\eta \sim 10^{-4}$, in line with theoretical works (e.g. Fujita et al. 2003; Cassano & Brunetti 2005, and references therein).

We show in the lower panels of Fig.10 the results obtained adopting different values of A_t (first three panels), and imposing a background magnetic field that scales with the gas density, as $B \propto \rho^{0.5}$, as suggested by both observations and cosmological simulations (e.g. Dolag & Stasyszyn 2009; Bonafede et al. 2010; Stasyszyn et al. 2010; Bonafede et al. 2011a,b). This shows the rather small range of parameters allowed by the morphological comparison, and supports the choice of our fiducial parameters for A_s and A_t . Considering that these simulations (Vazza et al. 2010) were not produced to fit this particular observation, it is remarkable that the final map of projected "radio" flux density - and its relation to the underlying X-ray emission - is so similar to the real observation of MACSJ1752.0+4440, both in produced morphologies and total power. It is not easy to relate the efficiency we derive, particularly the one for turbulence, to theoretical works, since we cannot model the small-scale coupling between turbulent MHD waves, relativistic particles and thermal plasma. Moreover, in these simulations we cannot follow the injection and advection of cosmic ray particles over time, and the production of secondary electrons (see however Vazza et al. 2012a). However, this test shows that a simple binary merger with a mass ratio of $\sim 1/3$ can reproduce the observation of MACSJ1752.0+4440 using a very tiny fraction ($\sim 10^{-5}$ at the relic and ~ 0.05 inside the halo) of the

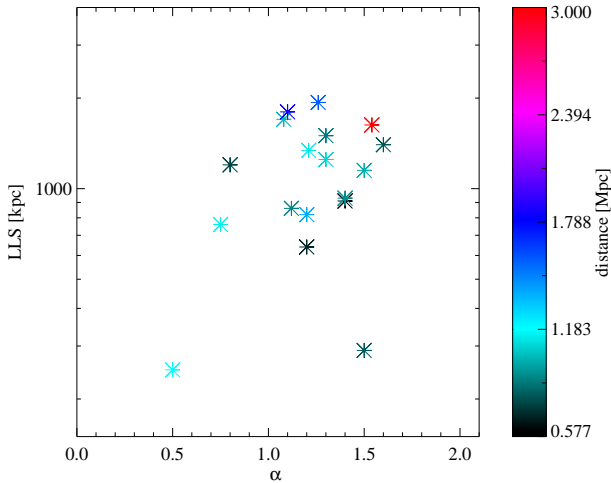


Figure 11. LLS- α correlation for relics in double-relics systems. In the on-line version of the paper the distance of the relics to the cluster centre is colour-coded.

energy dissipated at the shock and of the turbulent energy.

For the other clusters presented in this article, we have not found a good match with the available dataset of simulated clusters presented in Vazza et al. (2010, 2011a). Large cosmological runs, as the one presented here, typically have a limited time sampling, and hence the chance of finding a good match for a complex merger configuration with a high impact velocity are fairly low.

5 NEW CORRELATIONS

5.1 Double relics

Collecting data from the literature, van Weeren et al. (2009b) have found that the relic LLS correlates with the projected distance from the cluster centre (i.e. larger relics are mostly located at larger distances from the cluster centre), and that the spectral index anti-correlates with the relic LLS (i.e. smaller relics use to have steeper spectral indices). These correlations can be explained by the fact that the larger shock waves occur mainly in lower-density and lower-temperature regions, and have hence larger Mach numbers (Skillman et al. 2008; Vazza et al. 2009a). However, correlations that include measures of length are affected by projection effects. As mentioned by van Weeren et al. (2009b) another problem with their analysis is that possible “radio phoenixes” were also included (located close to the cluster centre and having very steep radio spectra). When two relics are observed in the same cluster, the most plausible scenario, in the framework of shock acceleration models, is that the merger is seen in the plane of the sky. Hence, projection effects should have the minimum impact on the measured lengths. In recent years the number of clusters with double relics has increased significantly. The data from the literature plus those presented in this work allow us now to look at the same correlations using only double relics clusters. This should reduce as much as possible the contamination by projection effects. Data have been corrected for the cosmology adopted in this paper, and the radio power has been computed at 1.4 GHz. The results are listed in Table 5. In cases where the spectral index was not available in the

literature, we assumed a spectral index $\alpha = 1.2$ in order to compute the radio power. These relics have not been considered for the spectral index correlations investigated below.

In Fig. 11 we show the $\alpha - \text{LLS}$ trend for double relics only. The distance is colour-coded, as in van Weeren et al. (2009b). In Fig. 12 the radio-power at 1.4 GHz is plotted versus the projected distance from the cluster centre, and versus the relic LLS. In these two plots the redshift of the host cluster is colour-coded. To investigate the existence of possible correlations between the plotted quantities, we use the Spearman’s Rank Correlation Coefficient (S-rank). The null hypotheses we are testing is the following: “ H_0 : there is no association between var_a and var_b .” We investigate separately a possible correlation between:

- $L_{1.4\text{GHz}}$ and distance from the cluster centre
- LLS and distance from the cluster centre
- LLS and $L_{1.4\text{GHz}}$
- LLS and α
- $L_{1.4\text{GHz}}$ and z

We have computed the S-rank and we have tested for correlations at the 5% level of significance (2-tail test). We find that the null hypotheses is accepted for $L_{1.4\text{GHz}}\text{-dist}$, LLS-dist, LLS- α , and $L_{1.4\text{GHz}} - z$, meaning that no correlation is significantly detected in these clusters at the 5% significance level. We note that if we apply the 1-tail test, the correlations $L_{1.4\text{GHz}}\text{-dist}$, LLS-dist, and $L_{1.4\text{GHz}} - z$ are found to be significant. Such a test is not accurate enough to establish a robust statistical correlation, but we argue that these correlations should be investigated using volume-complete samples. The null hypothesis is instead rejected for the correlations LLS- $L_{1.4\text{GHz}}$, meaning that the two variables are correlated at 5% significance level. Relics with high radio power tend to have larger linear sizes.

5.2 Radio halos

Giovannini et al. (2009) have compiled a list of the radio halos at $z < 0.4$ known to that date. In this work, we have more than doubled the radio halos in clusters at $z > 0.4$. Although the sample we have presented focuses on observations of the most promising candidates, and is not a statistical sample, it is interesting to compare the properties of higher and lower redshift radio halos. We have taken all the clusters in Giovannini et al. (2009) plus Abell 399 (Murgia et al. 2010), Abell 746, RXC J0107.8+5408 (van Weeren et al. 2011a), RXC J2003.5-2323, (Giacintucci et al. 2009), CL0016+16 (Giovannini & Feretti 2000), MACSJ0717+3745 (Bonafede et al. 2009a; van Weeren et al. 2009c), Abell 781 (Govoni et al. 2011, but see Venturi et al. 2011a for a different interpretation), Abell 1689 (Vacca et al. 2011), RXCJ1514.9-1523 (Giacintucci et al. 2011), Abell 1682 (Venturi et al. 2011b), Abell 523 (Giovannini et al. 2011), and 0217+70 (Brown et al. 2011a), plus those discovered in this work. The radio power has been computed at 1.4 GHz using the spectral indices available in the literature and assuming $\alpha = 1.3$ otherwise. In Fig. 13 the $L_{1.4\text{GHz}} - L_x$ correlation and the LLS- $L_{1.4\text{GHz}}$ correlations are shown. The $L_{1.4\text{GHz}} - L_x$ and LLS- $L_{1.4\text{GHz}}$ correlations are well known (e.g. Giovannini et al. 2009, and ref therein).

To investigate the apparent correlations between the LLS and

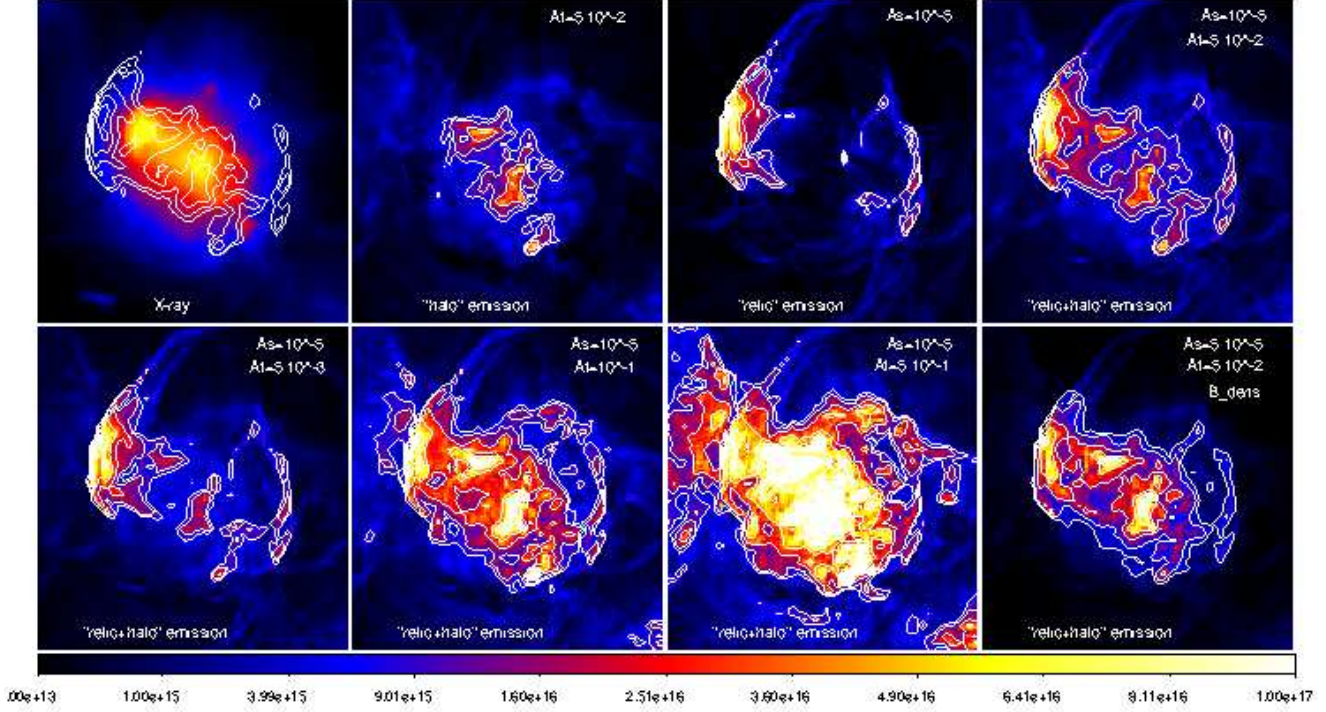


Figure 10. Mock observations for a simulated cluster at $z = 0.05$. Top left: projected X-ray flux in the [0.5-2] keV energy band (colours). In the remaining 3 panels of the same row: simulated halo, relic emission (colours, [10^{20} ergs $^{-1}$]) and relic+halo emission for the set of values $A_s = 10^{-5}$ and $A_t = 0.05$. The iso-contours are drawn similarly to the radio observation in Fig. 5 smoothing the numerical data over an equivalent beam size (we show them also in overlay with the X-ray colour map in the first panel, which should be compared with the left panel of Fig. 5). The efficiencies assumed for the production of synchrotron at shocks and turbulence are printed within the panel. Lower panels: observable radio emission from the same region, assuming different efficiencies for shocks and turbulence, or a background magnetic field that scales with the gas density as $B \propto \rho^{0.5}$.

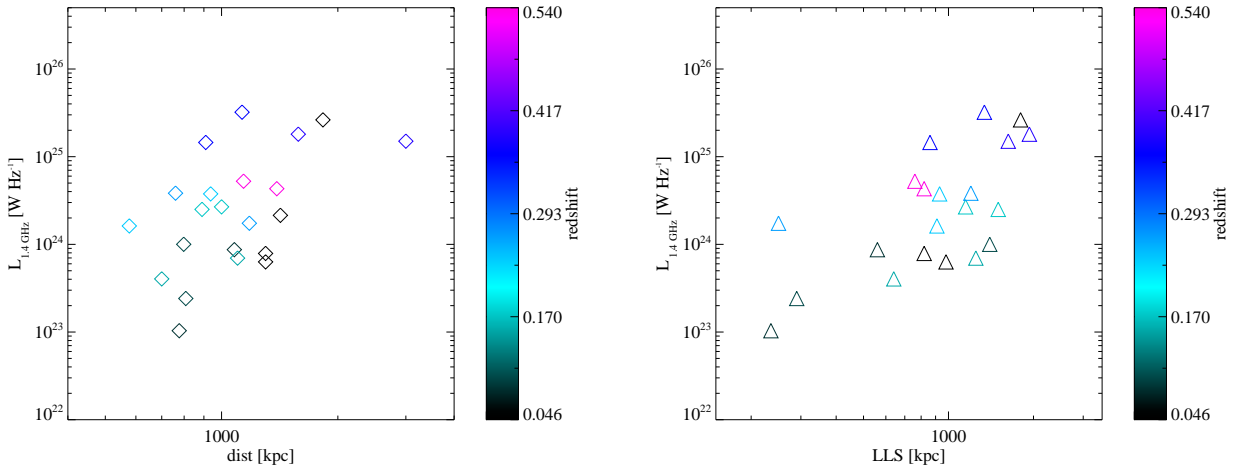


Figure 12. Radio power of double relics vs distance from the cluster centre (left) and versus the relic LLS (right). In the on-line version of the paper the redshift of the hosting cluster is colour-coded.

the cluster redshift and between the $L_{1.4\text{GHz}}$ and the cluster redshift, we have computed the S-rank. Using a 2-tail test the correlations are confirmed with a 1% level of significance, but we are aware that several observational biases have to be considered: high- z samples, as MACS, cover a volume that is larger than low- z ones, making it easier to pick-up the most extreme systems, and less pow-

erful objects are more difficult to detect at high z . On the other hand, extended radio halos at low z could be resolved out by interferometers (see Fig. 15 in Giovannini et al. 2009). Hence, complete statistical samples covering similar volumes, and free from the above mentioned biases should be used to test the correlation. If confirmed, this correlation would further support the radio-halo

Table 5. Properties of double relics from the literature and this work.

name	z	freq GHz	flux mJy	err flux mJy	alpha	$L_{1.4}$ GHz W Hz ⁻¹	LLS kpc	dist kpc	Lx [0.1-2.4] 10 ⁴⁴ erg s ⁻¹	ref
A3365 E	0.0926	1.4	42	3	-	8.7e+23	560	1079	0.859	vW11a
A3365 W	0.0926	1.4	5	0.5	-	1.0e+23	235	777	0.859	vW11a
ZwCl0008.8+5215 E	0.103	1.4	37	3	1.6	1.0e+24	1400	798	0.5	vW11b
ZwCl0008.8+5215 W	0.103	1.4	9	1	1.5	2.4e+23	290	808	0.5	vW11b
A1240 N	0.1590	1.4	6.0	0.2	1.2	4.0e+23	640	700	1.0	B09
A1240 S	0.1590	1.4	10.2	0.4	1.3	7.0e+23	1250	1100	1.0	B09
A2345 E	0.1765	1.4	29.0	0.4	1.3	2.5e+24	1500	890	5.3	B09
A2345 W	0.1765	1.4	30.0	0.5	1.5	2.7e+24	1150	1000	5.3	B09
RXCJ1314.4-2515 E	0.2439	0.6	28.0	1	1.4	1.6e+24	910	577	10.9	V,F
RXCJ1314.4-2515 W	0.2439	0.6	65	3	1.4	3.7e+24	910	937	10.9	V,F
MACSJ1149.5+2223 E	0.54	0.3	29	3	1.2	5.4e+24	820	1390	14.0	*
MACSJ1149.5+2223 W	0.54	0.3	29	3	0.8	9.0e+24	760	1140	14.0	*
MACSJ1752.0+4440 NE	0.366	1.7	55	3	1.21	3.2e+25	1340	1130	8.2	vW12, *
MACSJ1752.0+4440 SW	0.366	1.7	26	1	1.13	1.4e+25	860	910	8.2	vW12, *
0217+70 E	0.065	1.4	-	-	1.76	-	-	1000	-	Br
0217+70 W	0.065	1.4	-	-	1.46	-	-	1000	-	Br
A3376 E	0.046	1.4	166	8.3*	-	7.9e+23	820	~1300	2.12	Ba06
A3376 W	0.046	1.4	133	6.7*	-	6.3e+23	980	~1300	2.12	Ba06
A3667 E	0.056	1.4	300	0.2	-	2.1e+24	1420	1420	9.3	R,JH
A3667 W	0.056	1.4	3700	300	2	2.6e+25	1800	1830	9.3	R, JH
CIZAJ2242.8+5301 N	0.192	1.4	-	-	1.08	-	1700	1030	6.8	vW10
CIZAJ2242.8+5301 S	0.192	1.4	-	-	-	-	1450	1520	6.8	vW10
ZwCl2341.1+0000 N	0.27	0.6	14	3	0.5	3.8e+24	250	1180	-	G/vW09
ZwCl2341.1+0000 S	0.27	0.6	37	13	0.8	1.7e+24	1200	760	-	G/vW09
PLCKG287.0+32.9 N	0.39	0.15	550	50	1.26	1.8e+25	1934	1580	17.2	Ba11
PLCKG287.0+32.9 S	0.39	0.15	780	50	1.54	1.5e+25	1628	3000	17.2	Ba11

Col. 1: Relic name, Col 2: redshift; Col. 3; frequency at which the flux density is measured

Col. 4 radio flux; Col. 5: error on the measured flux; Col. 6: spectral index;

Col. 7 Radio power at 1.4 GHz. When α was not available we have assumed $\alpha=1.2$

Col. 8: Largest Linear Size of the radio emission; Col 9: Distance from the cluster centre

Col. 10: X-ray luminosity in the 0.1- 2.4 keV band; Col. 11: reference for the radio emission

* This work,

B09 (Bonafede et al. (2009b),

vW11a (van Weeren et al. 2011a),

vW11b (van Weeren et al. 2011b),

vW10 (van Weeren et al. 2010),

vW09 (van Weeren et al. 2009a),

V (Venturi et al. 2007),

F (Feretti et al. 2005),

vW12 (van Weeren et al. 2012a)

Br (Brown et al. 2011a),

Ba06 (Bagchi et al. 2006),

R (Rottgering et al. 1997),

JH (Johnston-Hollitt 2004),

vW10 (van Weeren et al. 2010),

G (Giovannini et al. 2010),

vW09 (van Weeren et al. 2009a),

Ba11 (Bagchi et al. 2011).

merging paradigm. In fact, major mergers between massive clusters are expected to take place in the redshift range $z > 0.3 - 0.4$. The power of radio halos could hence trace the quantity of energy injected in the ICM during the cosmic time. The dependence of the halo's LLS from the cluster redshift is not trivial to explain. As the redshift increases, also the IC equivalent field increases, so that one should expect higher z objects to be more dominated by IC emission compared to the local ones. Hence, this correlation might hint towards a mechanism that is more efficient at the cluster outskirts at higher z . However, complete statistical samples covering similar

volumes and free of biases are needed to draw any firm conclusions on this.

6 CONCLUSIONS

We have presented new radio observations of massive galaxy clusters located at high redshift ($z > 0.3$). Our GMRT observations combined with WSRT and archival VLA observations have lead

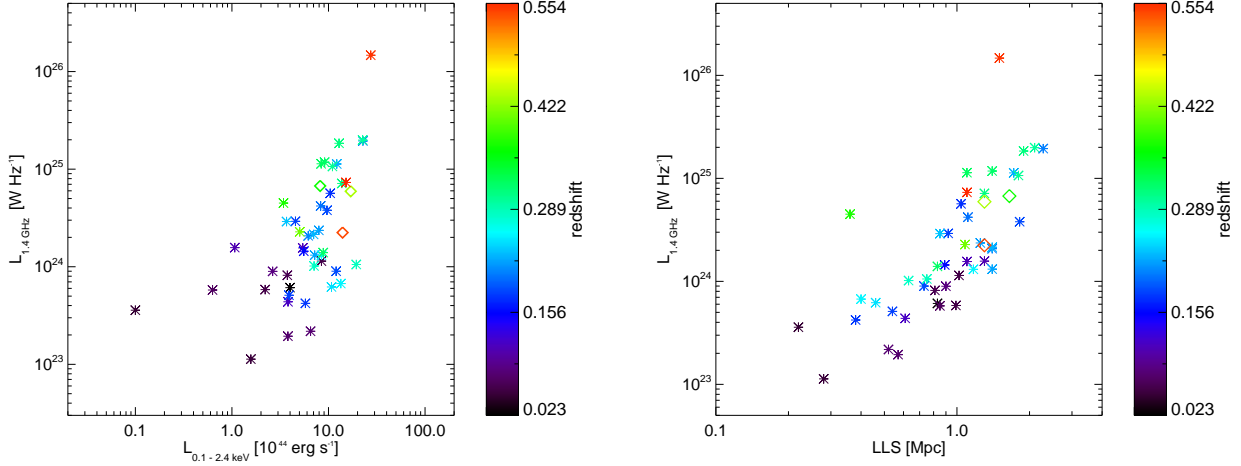


Figure 13. Left panel: Correlations between the radio halo power at 1.4 GHz ($L_{1.4\text{GHz}}$) and the cluster X-ray Luminosity computed in the 0.1-2.4 keV energy band (L_x). Right panel: Correlations between the radio halo power at 1.4 GHz ($L_{1.4\text{GHz}}$) and the Largest Linear Scale of the radio emission. In the on-line version of the paper the redshift is colour-coded. The newly discovered radio halos are marked with diamonds.

to the discovery of two radio halos, 2 double-relic systems and a candidate radio halo. Our results can be summarized as follows:

- Two radio relics and a candidate radio halo are detected in the cluster MACSJ1149.5+2223, at $z = 0.54$. This is the most distant cluster with double relics detected so far, and it shows peculiar features that have never been observed in other galaxy clusters. The relics have a total extent of ~ 800 kpc and are located at 1.1 and 1.4 Mpc from the cluster centre, where the X-ray brightness drops down. The position of the relics is peculiar, and misaligned with the cluster merger axis. We argue that this peculiar feature could be a sign of additional merging in this complex system. In the framework of DSA, the integrated spectral indices of the relics indicate Mach numbers $M \sim 3$ and 4.6. The relics show an average polarization of 5%, with polarization values up to 30%. The polarization vectors suggest a magnetic field roughly oriented along the relics' main axes. The candidate radio halo has a total extent of ~ 1.3 Mpc, and a radio flux density of ~ 29 mJy at 323 MHz. The radio halo is barely visible in the VLA image. The spectral index α is larger than 2, making it the radio halo with the steepest spectrum known so far.

- In the cluster MACSJ1752.0+4440 ($z = 0.366$) two radio relics and a radio halo are detected at 323 MHz. Their existence was already suggested by Edge et al. (2003) and confirmed by WSRT observations (van Weeren et al. 2012a). The relics have a total extent of 1.1 and 0.9 Mpc, and are symmetric about the cluster centre. The relics in this cluster are a text-book example for shock acceleration. The spectral index trends derived between 1.7 GHz and 323 MHz show a clear steepening toward the cluster centre, possibly tracing the particle aging as we move far from the shock front. Assuming that the flattest spectral indices are representative of the injected spectrum of the particles, we derive $M \sim 4.6$ and 2.8, in agreement with Mach numbers expected for merging shocks in the outskirts of galaxy clusters. The relics are polarized on average at a 20% level, and show stronger polarization - up to 40% - in the outer parts. The polarization vectors indicate an ordered magnetic field mainly aligned with the relic main axes, in line with model predictions. The radio halo has an irregular morphology. Its emission is elongated along the NE-SW direction, connected with the

relics' emission. The brightest radio halo regions do not correspond to the brightest X-ray regions of the cluster. The spectral index of the radio halo between 323 MHz and 1.7 GHz is $\alpha = 1.33 \pm 0.07$.

- A radio halo is discovered in the cluster MACSJ0553.4-3342, at $z = 0.431$. Its total extent is ~ 1.3 Mpc. The halo is elongated in the EW direction, along the merger axes. The merger between two sub-clusters is likely to lie close to the plane of the sky, and the two cores have just passed each other. Given the small separation between the two X-ray cores, we derive that they passed each other ~ 0.08 Gyr ago. If turbulent (re)acceleration is responsible for the halo emission, then turbulent motions must have developed well in time before the impact of the two cores. While the merger is violent enough to power a radio halo, we note the absence of radio relics in this systems and speculate about the reasons.

- From a set of high-resolution cosmological simulations we have picked a cluster whose projected X-ray surface brightness and morphology is similar to MACSJ1752.0+4440. We have assumed that the energy is converted from shocks to radio emission with an efficiency A_s , defined such that the radio power, P_{relic} is equal to $A_s \cdot \Phi_{\text{shock}}$, and for turbulence with an efficiency A_t such that the halo power is $P_{\text{halo}} \sim A_t \Phi_{\text{turb}}$, where Φ_{shock} and Φ_{turb} is the energy flux from relativistic electrons accelerated by shocks and turbulence, respectively. Adopting simple recipes, we are able to reproduce both the radio power and the observed morphology of the relic emission by assuming $A_s \approx 10^{-5}$. In order to match the power and morphology of the radio halo we require instead $A_s \approx 0.05$. This conversion factor corresponds to an efficiency of turbulent acceleration of $\eta \sim 10^{-4}$. In both cases only a very tiny fraction of the energy supplied by the merger is required to explain the observed radio emission.

- We have investigated the LLS- α , distance- α , $L_{1.4\text{GHz}}$ - distance, LLS-distance, and $L_{1.4\text{GHz}} - z$ correlations for radio relics. We have considered only double-relics systems to minimize projection effects. We find no statistical evidence for such correlation at 5% level of significance (2-tail test). We have found a correlation between double relics LLS and the relic radio power (LLS- $L_{1.4\text{GHz}}$ correlation). We note that the correlations $L_{1.4\text{GHz}}$ - distance, LLS-distance, and $L_{1.4\text{GHz}} - z$ would be accepted if we applied a 1-tail test at 5% level of significance. We do not consider here

such test to be accurate enough to probe a robust statistical correlation, but we argue that complete samples of double-relic clusters are needed to understand whether these correlations are present or not.

- Collecting published data on radio halos, we find that the power of radio halos correlates with the redshift of the host cluster ($L_{1.4\text{GHz}} - z$ correlation). Since the most powerful mergers are expected at $z > 0.3 - 0.4$, this correlation indicates a link between the energy injected in the ICM and the particle acceleration efficiency and/or magnetic field amplification. The LLS of the radio halo is also found to correlate with the cluster's redshift (LLS- z correlation). This correlation is not easily explained since ultra-relativistic particles lose more energy through the IC mechanism as the redshift increases. Although several observational biases can affect such correlations, we argue that, if confirmed, they would provide some clues about the redshift-dependence of the particle acceleration mechanism.

Acknowledgments We thank the referee, Shea Brown, for his useful comments on the manuscript. AB, MB, FV, MH, and UK acknowledge support by the research group FOR 1254 funded by the Deutsche Forschungsgemeinschaft: “Magnetization of interstellar and intergalactic media: the prospect of low frequency radio observations”. We thank the staff of the GMRT that made these observations possible. GMRT is run by the National Centre for Radio Astrophysics of the Tata Institute of Fundamental Research. This research has made use of the NASA/IPAC Extragalactic Data Base (NED) which is operated by the JPL, California institute of Technology, under contract with the National Aeronautics and Space Administration. We thank G. Macario, G. Brunetti, and R. Cassano for useful discussions. FV acknowledges the usage of computational time under the INAF-CINECA agreement, and acknowledges C. Gheller for fruitful collaboration in the production of the simulations. HE acknowledges financial support from SAO grants GO1-12153X.

REFERENCES

- Baars J. W. M., Genzel R., Pauliny-Toth I. I. K., Witzel A., 1977, *A&A*, 61, 99
- Bagchi J., Durret F., Neto G. B. L., Paul S., 2006, *Science*, 314, 791
- Bagchi J. et al., 2011, *ApJ*, 736, L8
- Basu K., 2012, *MNRAS*, 421, L112
- Battaglia N., Pfrommer C., Sievers J. L., Bond J. R., Enßlin T. A., 2009, *MNRAS*, 393, 1073
- Becker R. H., White R. L., Helfand D. J., 1995, *ApJ*, 450, 559
- Blandford R., Eichler D., 1987, *Phys. Rep.*, 154, 1
- Böhringer H. et al., 2004, *A&A*, 425, 367
- Böhringer H. et al., 2000, *ApJS*, 129, 435
- Bonafede A., Dolag K., Staszczyn F., Murante G., Borgani S., 2011b, *MNRAS*, 418, 2234
- Bonafede A. et al., 2009a, *A&A*, 503, 707
- Bonafede A., Feretti L., Murgia M., Govoni F., Giovannini G., Dallacasa D., Dolag K., Taylor G. B., 2010, *A&A*, 513, A30
- Bonafede A., Giovannini G., Feretti L., Govoni F., Murgia M., 2009b, *A&A*, 494, 429
- Bonafede A., Govoni F., Feretti L., Murgia M., Giovannini G., Brügger M., 2011a, *A&A*, 530, A24+
- Brown S., Duisterhoeft J., Rudnick L., 2011a, *ApJ*, 727, L25
- Brown S., Emerick A., Rudnick L., Brunetti G., 2011b, *ApJ*, 740, L28
- Brügger M., Bykov A., Ryu D., Röttgering H., 2011, *Space Science Reviews*, 138
- Brunetti G. et al., 2008, *Nature*, 455, 944
- Brunetti G., Setti G., Feretti L., Giovannini G., 2001, *MNRAS*, 320, 365
- Buote D. A., 2001, *ApJ*, 553, L15
- Cassano R., Brunetti G., 2005, *MNRAS*, 357, 1313
- Cassano R., Ettori S., Giacintucci S., Brunetti G., Markevitch M., Venturi T., Gitti M., 2010, *ApJ*, 721, L82
- Cavagnolo K. W., Donahue M., Voit G. M., Sun M., 2008, *ApJ*, 682, 821
- Collins D. C., Xu H., Norman M. L., Li H., Li S., 2010, *ApJS*, 186, 308
- Condon J. J., Cotton W. D., Greisen E. W., Yin Q. F., Perley R. A., Taylor G. B., Broderick J. J., 1998, *AJ*, 115, 1693
- Dallacasa D. et al., 2009, *ApJ*, 699, 1288
- Dennison B., 1980, *ApJ*, 239, L93
- Dolag K., Staszczyn F., 2009, *MNRAS*, 398, 1678
- Donnert J., Dolag K., Brunetti G., Cassano R., Bonafede A., 2010, *MNRAS*, 401, 47
- Ebeling H., Barrett E., Donovan D., Ma C.-J., Edge A. C., van Speybroeck L., 2007, *ApJ*, 661, L33
- Ebeling H., Edge A. C., Allen S. W., Crawford C. S., Fabian A. C., Huchra J. P., 2000, *MNRAS*, 318, 333
- Ebeling H., Edge A. C., Henry J. P., 2001, *ApJ*, 553, 668
- Ebeling H., Edge A. C., Mantz A., Barrett E., Henry J. P., Ma C. J., van Speybroeck L., 2010, *MNRAS*, 407, 83
- Edge A. C., Ebeling H., Bremer M., Röttgering H., van Haarlem M. P., Rengelink R., Courtney N. J. D., 2003, *MNRAS*, 339, 913
- Enßlin T., Pfrommer C., Miniati F., Subramanian K., 2011, *A&A*, 527, A99
- Ensslin T. A., Biermann P. L., Klein U., Kohle S., 1998, *A&A*, 332, 395
- Feretti L., Schuecker P., Böhringer H., Govoni F., Giovannini G., 2005, *A&A*, 444, 157
- Ferrari C., Govoni F., Schindler S., Bykov A. M., Rephaeli Y., 2008, *Space Science Reviews*, 134, 93
- Fujita Y., Takizawa M., Sarazin C. L., 2003, *ApJ*, 584, 190
- Giacintucci S., Dallacasa D., Venturi T., Brunetti G., Cassano R., Markevitch M., Athreya R. M., 2011, *A&A*, 534, A57
- Giacintucci S., Venturi T., Brunetti G., Dallacasa D., Mazzotta P., Cassano R., Bardelli S., Zucca E., 2009, *A&A*, 505, 45
- Giovannini G., Bonafede A., Feretti L., Govoni F., Murgia M., 2010, *A&A*, 511, L5
- Giovannini G., Bonafede A., Feretti L., Govoni F., Murgia M., Ferrari F., Monti G., 2009, *A&A*, 507, 1257
- Giovannini G., Feretti L., 2000, *New Astr.*, 5, 335
- Giovannini G., Feretti L., Girardi M., Govoni F., Murgia M., Vacca V., Bagchi J., 2011, *A&A*, 530, L5
- Giovannini G., Feretti L., Venturi T., Kim K.-T., Kronberg P. P., 1993, *ApJ*, 406, 399
- Govoni F., Feretti L., Giovannini G., Böhringer H., Reiprich T. H., Murgia M., 2001, *A&A*, 376, 803
- Govoni F., Murgia M., Giovannini G., Vacca V., Bonafede A., 2011, *A&A*, 529, A69
- Hoefl M., Brügger M., 2007, *MNRAS*, 375, 77
- Iapichino L., Brügger M., 2012, *ArXiv e-prints*
- Johnston-Hollitt M., 2004, in *The Riddle of Cooling Flows in Galaxies and Clusters of galaxies*, T. Reiprich, J. Kempner, & N. Soker, ed., p. 51

- Kang H., Ryu D., 2011, *ApJ*, 734, 18
- Keshet U., Loeb A., 2010, *ApJ*, 722, 737
- Liang H., Hunstead R. W., Birkinshaw M., Andreani P., 2000, *ApJ*, 544, 686
- Macario G., Markevitch M., Giacintucci S., Brunetti G., Venturi T., Murray S. S., 2011, *ApJ*, 728, 82
- Mann A. W., Ebeling H., 2012, *MNRAS*, 420, 2120
- Markevitch M., Govoni F., Brunetti G., Jerius D., 2005, *ApJ*, 627, 733
- McMahon R. G., White R. L., Helfand D. J., Becker R. H., 2002, *ApJS*, 143, 1
- Murgia M., Govoni F., Feretti L., Giovannini G., 2010, *A&A*, 509, A86
- Nuza S. E., Hoeft M., van Weeren R. J., Gottlöber S., Yepes G., 2012, *MNRAS*, 420, 2006
- Oppermann N. et al., 2011, *ArXiv e-prints*
- Perley R. T., Taylor G. B., 1999, *VLA Calibrator Manual*, Tech. rep. NRAO
- Pfrommer C., Springel V., Enblin T. A., Jubelgas M., 2006, *MNRAS*, 367, 113
- Poole G. B., Fardal M. A., Babul A., McCarthy I. G., Quinn T., Wadsley J., 2006, *MNRAS*, 373, 881
- Röttgering H. J. A., Wieringa M. H., Hunstead R. W., Ekers R. D., 1997, *MNRAS*, 290, 577
- Russell H. R. et al., 2011, *MNRAS*, 417, L1
- Sarazin, C. L., 1999, *X-ray emission from cluster of galaxies*. Cambridge Astrophysics Series
- Siejkowski H., Soida M., Otmianowska-Mazur K., Hanasz M., Bomans D. J., 2010, *A&A*, 510, A97+
- Skillman S. W., Hallman E. J., O'Shea B. W., Burns J. O., Smith B. D., Turk M. J., 2011, *ApJ*, 735, 96
- Skillman S. W., O'Shea B. W., Hallman E. J., Burns J. O., Norman M. L., 2008, *ApJ*, 689, 1063
- Smith G. P. et al., 2009, *ApJ*, 707, L163
- Solovyeva L., Anokhin S., Feretti L., Sauvageot J. L., Teyssier R., Giovannini G., Govoni F., Neumann D., 2008, *A&A*, 484, 621
- Staszczyn F., Nuza S. E., Dolag K., Beck R., Donnert J., 2010, *MNRAS*, 408, 684
- Vacca V., Govoni F., Murgia M., Giovannini G., Feretti L., Tugnoli M., Verheijen M. A., Taylor G. B., 2011, *A&A*, 535, A82
- van Weeren R. J., Bonafede A., Ebeling H., Edge A. C., Brügger M., Giovannini G., Hoeft M., Röttgering H. J. A., 2012a, *ArXiv e-prints*
- van Weeren R. J., Brügger M., Röttgering H. J. A., Hoeft M., Nuza S. E., Intema H. T., 2011a, *A&A*, 533, A35
- van Weeren R. J., Hoeft M., Röttgering H. J. A., Brügger M., Intema H. T., van Velzen S., 2011b, *A&A*, 528, A38
- van Weeren R. J. et al., 2009a, *A&A*, 506, 1083
- van Weeren R. J., Röttgering H. J. A., Brügger M., 2011c, *A&A*, 527, A114
- van Weeren R. J., Röttgering H. J. A., Brügger M., Cohen A., 2009b, *A&A*, 508, 75
- van Weeren R. J., Röttgering H. J. A., Brügger M., Cohen A., 2009c, *A&A*, 505, 991
- van Weeren R. J., Röttgering H. J. A., Brügger M., Hoeft M., 2010, *Science*, 330, 347
- van Weeren R. J. et al., 2012b, *ArXiv e-prints*
- Vazza F., Brügger M., Gheller C., Brunetti G., 2012a, *MNRAS*, 421, 2518
- Vazza F., Brügger M., van Weeren R., Bonafede A., Dolag K., Brunetti G., 2012b, *MNRAS*, 421, 1868
- Vazza F., Brunetti G., Gheller C., 2009a, *MNRAS*, 395, 1333
- Vazza F., Brunetti G., Gheller C., Brunino R., 2010, *New Astr.*, 15, 695
- Vazza F., Brunetti G., Gheller C., Brunino R., Brügger M., 2011a, *A&A*, 529, A17+
- Vazza F., Brunetti G., Kritsuk A., Wagner R., Gheller C., Norman M., 2009b, *A&A*, 504, 33
- Vazza F., Dolag K., Ryu D., Brunetti G., Gheller C., Kang H., Pfrommer C., 2011b, *MNRAS*, 418, 960
- Vazza F., Roediger E., Brügger M., 2012c, *ArXiv e-prints*
- Venturi T., Giacintucci S., Dallacasa D., Brunetti G., Cassano R., Macario G., Athreya R., 2011a, *MNRAS*, 414, L65
- Venturi T., Giacintucci S., Brunetti G., Cassano R., Bardelli S., Dallacasa D., Setti G., 2007, *A&A*, 463, 937
- Venturi T., Giacintucci S., Dallacasa D., 2011b, *Journal of Astrophysics and Astronomy*, 32, 501
- Venturi T., Giacintucci S., Dallacasa D., Cassano R., Brunetti G., Bardelli S., Setti G., 2008, *A&A*, 484, 327
- Voges W., Aschenbach B., Boller T., Bräuninger H. e. a., 1999, *A&A*, 349, 389